MICRODRILLING OF NITINOL

A Thesis

by

STEPHEN WELLS

Submitted to the Office of Graduate and Professional Studies of
Texas A&M University
in partial fulfillment of the requirements for the degree of

MASTER OF SCIENCE

Chair of Committee,	Wayne N.P. Hung
Co-Chair of Committee,	Steve Suh
Committee Member,	Theofanis Strouboulis
Head of Department,	Andreas Polycarpou

December 2013

Major Subject: Mechanical Engineering

ABSTRACT

Nitinol, a shape memory alloy, has seen increased use in a variety of industries, especially the medical industry due to its biocompatibility. The growing demand for product miniaturization combined with these newfound uses has accelerated the need for scientific research into microdrilling. Conventional microdrilling in particular shows promise for its ability to produce accurate, high quality holes in a cost efficient manner when compared to other technologies.

This research investigated the minimization of tool wear when drilling with Ø127µm uncoated tungsten carbide tools, as well as with AlTiN/Si3N_4 and AlTiN coated tools in minimum quantity lubrication condition. The proper and optimal coatings protected the tool surface and reduced tool wear at higher cutting speeds but were ineffective at lower cutting speeds. Additionally, control of built up edge formation proved critical in decreasing wear, reducing drill wandering and improving hole quality.

Finite element analysis was used with the orthogonal cutting model to predict tool fracture as a function of cutting speed and chip load. The method provided reasonable estimates of cutting and axial forces involved in the microdrilling process, but failed to predict the formation of built up edge and its effect.

ACKNOWLEDGEMENTS

I would like to express my gratitude to Dr. Hung for his guidance and patience with me throughout the course of this research. I have learned a lot by working with him, and the past two years were very enjoyable. My committee members Dr. Strouboulis and Dr. Suh also provided much technical assistance over the last two years, particularly in the study of finite element analysis and setting up my experiments, and I thank them as well.

I would also like to thank Adam Farmer, Sankalp Mohanty, and Dominic Shiosaki for their invaluable assistance in setting up the experiments and teaching me all they could about micromachining. Sincere thanks to our sponsors PMT Corporation, Swiss Tek Coating, UNIST, and Haas Automation for their donation of tools and equipment that was critical to my research.

Lastly, I want to say thanks to my wife McKinlea and the rest of my family for their love and support, and for all of their encouragement. Gloria in excelsis Deo.

TABLE OF CONTENTS

Page

Page

LIST OF FIGURES

Page

Page

Page

LIST OF TABLES

Page

LIST OF SYMBOLS AND ACRONYMS

α	Rake Angle (°)
A_c	Compression Area (μm^2)
A_S	Shear Area (μm^2)
β	Friction Angle (°)
F_A	Axial Force (N)
F_C	Cutting Force (N)
F_S	Shear Force (N)
F_T	Thrust Force (N)
F'_T	Compressive Force (N)
μ	Coefficient of Friction
Φ	Shear Angle (°)
S	Spindle Speed (rpm)
S_c	Compression Strength (MPa)
S_s	Shear Strength (MPa)
t_o	Chip Load (µm)
Vc	Cutting Speed (m/min)
V	Drop Volume (µL)
w	Cutting Edge Width (µm)

BUE	Built Up Edge
EDM	Electrical Discharge Machining
HV	Vickers Hardness
FEA	Finite Element Analysis
MQL	Minimum Quantity Lubrication
UTS	Ultimate Tensile Strength (MPa)

1. INTRODUCTION

The increasing demand for product miniaturization has the pushed the boundaries of our manufacturing knowledge to the limit, thus requiring the development of new and novel techniques to produce the desired results. The use of Nitinol in the medical and aerospace industries in particular has spurred researchers around the world to investigate its unique properties in order to develop more cost efficient methods of manufacture.

Machining of Nitinol has been studied extensively since its discovery in 1959 (Gould 1963), yet there has been little research into conventional micromachining, especially microdrilling. Nitinol is known as a difficult material to machine (Huang 2004), and while one might consider that the cutting parameters discovered in early research could be scaled down to the micro level, the simple fact is that there are many new issues introduced when working on such a small scale, making this impossible. The scope of this study is to:

1.) Explore the effects of cutting speed and chip load on microdrilling using coated and uncoated tungsten carbide microtools. Cutting tools are analyzed for effective coating/lubricants of tool and workpiece materials.
2.) Investigate the quality of drilled holes.
3.) Develop a finite element model to help predict the maximum loads a microdrill can endure before failure.

2. LITERATURE REVIEW

2.1 Nitinol

Nitinol is a unique metal in that it possesses a “shape memory” effect. Its name is derived from its chemical composition -nickel and titanium- and its place of discovery in 1959, the Naval Ordinance Laboratory (Kauffman and Mayo 1996). The shape memory effect is the ability to withstand plastic deformation at one temperature, and still return to its pre-deformed state when heated above its transitional temperature. This effect originates from a martensitic phase transformation without diffusion (Lendlein and Kelch 2002). The martensitic phase is created by cooling the metal from a higher temperature austenitic phase with simple cubic structure down to a lower temperature phase with a monoclinic crystal structure.

The shape of the material can be set by heat treating to approximately 500 °C (in the austenitic phase) and holding it in its desired shape for 10-20 minutes; rapidly cooling the material by water quenching or rapid air cooling will now produce a usable shape in a martensitic phase (Kauffman and Mayo 1996). Upon subsequent deformation and heating, the material will return to the austenitic phase where it then assumes the shape that was originally set (see Figure 1).

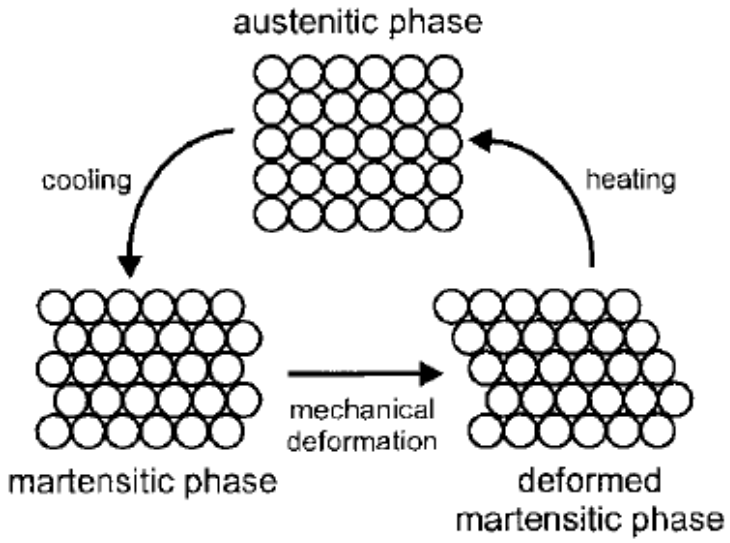

Figure 1: Schematic of the shape memory effect (Lendlein and Kelch 2002)

The shape memory process is highly sensitive to small changes in the stoichiometry of the material. A deviation of 1 atom% can change the transition temperature up to 100K (Lendlein and Kelch 2002). This allows the material's transition temperature to be carefully tuned to fit its desired use – for example, a variety of biological implants can be constructed to be activated by the body's heat at 37 °C.

This remarkable shape memory trait lends itself to a wide variety of uses, the first of which becoming commercially viable as hydraulic couplings in the Grumman F-14 fighter in 1969. The couplings were cooled with liquid nitrogen and formed to the desired shape, and then placed around the tubing and allowed to reheat to room temperature. The Nitinol would then expand and create a tight seal around the tubing, preventing any fluid from escaping (Kauffman and Mayo 1996). Furthermore, Nitinol is biocompatible, which lends itself well to various medical applications, including stents,

orthodontic wires, surgical instruments for minimally invasive processes, staples for realigning broken bones, and glasses frames (Pelton, Stockel, and Duerig 2000). This biocompatibility in large part is due to passivation which forms a layer of TiO_2 on the surface of the material. This layer, which is formed in other Ti alloys, provides a barrier to corrosion of the bulk material and helps prevent the oxidation of Ni, which can be toxic (Shabalovskaya 2002).

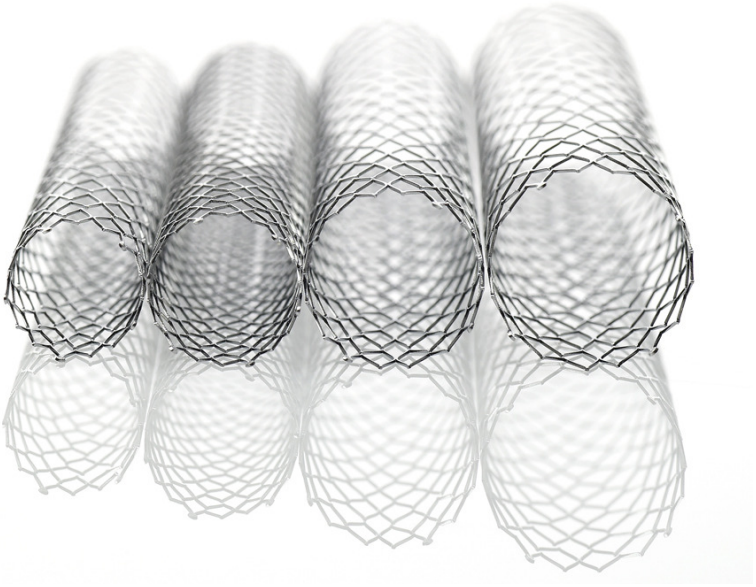

Figure 2: Nitinol stents in varying sizes (Covidien 2012)

2.2 Micromachining

The development of micromachining tools and processes has followed the demand for higher precision, reduced weight and dimensions, and decreased costs (Dormfeld, Min, and Takeuchi 2006). This demand is driven by several key industries, including automotive, medical, electronics, and aerospace. With the advent of computer

numerical control milling machines, precise control of the tool allows the user to develop workpieces in the range of 10 to 100 µm (Byrne, Dornfeld, and Denkena 2003). While there are other techniques that can produce microholes, such as electrical discharge micromachining (EDM), laser drilling, and chemical etching, there are concerns about poor surface integrity and hole definition (Imran et al. 2008).

Electrical discharge machining can produce subsurface damage as well as poor surface quality due to repeated sparking, and will yield undesirable dimensions as the electrode wears. Laser drilling equipment is very expensive, and the thermal interaction between the workpiece and the laser can result in a change of mechanical properties in the heat affected zone. Laser drilling also tends to give poor hole definition and surface finish. Chemical etching involves the use of acids to erode the surface of the workpiece, with the depth of cut being controlled by the concentration of acid and time. This technique, however, has issues with producing straight walls. Conventional microdrilling can produce holes with good roundness, straightness, and surface quality with short processing times, making it an attractive manufacturing method (Allen, Almond, and Logan 2000).

2.2.1 Conventional Microdrilling Challenges

When compared to macrodrilling, a microdrill experiences greater wandering motion, as well as an increased susceptibility to deformation by bending, buckling, and torsion (Imran et al. 2008). As a result, forces acting on a microdrill will often result in tool breakage. One major contributor to these high cutting forces is a result of cutting edge wear or formation of built up edge (BUE). When the edges become dull, the drill is

unable to remove enough material for the center of the tool, causing the tool to deflect. This deflection can create excessive stresses, leading to failure (Tansel et al. 1998). Studies showed constant increase of the cutting force during machining due to increased tool wear, so monitoring these forces can provide an indication of when the tool will fail. Unfortunately, monitoring these forces proves difficult to do with micro tools because the forces are very small and not easy to discern from the noise of electric signals (Ueng, Guo, and Dittrich 2006).

Another major challenge to microdrilling is determining proper cutting conditions. While there is much literature available for cutting on the macro level, these parameters do not scale down to the micro level due to size effects. When the grain size and undeformed chip thickness become comparable to the tool radius, the cutting mechanics of microdrilling differ from working on the macro scale (Imran et al. 2008). Tool runout also becomes an issue due to size effects with microdrilling. On the macro scale, this is typically not an issue, but any eccentricity can affect the positional accuracy of the drill. At the micro scale this can lead to out of spec parts (Martin and Wilcox 1990).

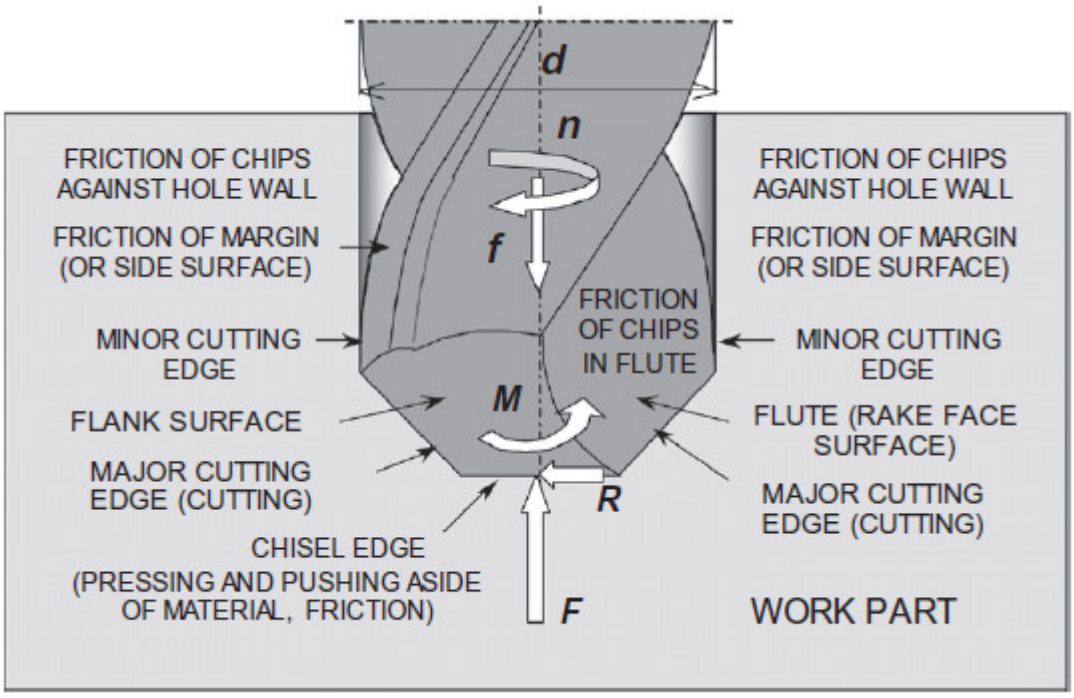

Figure 3: Cutting forces and phenomena (Kudla, 2011)

One important wear mechanism is chip clogging, which causes cutting forces and stresses to increase rapidly, resulting in early tool breakage. This makes it essential to have a pecking drill cycle when drilling holes with a high aspect ratio, and to have an adequate supply of cutting fluid to flush the chips away. Flood coolant that is commonly used in macro machining is not ideal for microdrilling for a number of reasons (Dormfeld, Min, and Takeuchi 2006). First, high flow pressure of the lubricants can influence the behavior of the micro drill. The force from the lubricant impacting the drill can result in a wandering motion, leading to poor hole quality and even tool breakage. Second, removal of excess fluid becomes an issue when machining at the micro level even with minimal cutting fluid flow rate. Third, when operating at high cutting speeds,

flood lubricant often fails to penetrate the boundary layer of the rotating tool, resulting in poor heat removal (Thamizhmanii, Rosli, and Hasan 2009).

2.2.2 Cutting Fluids

To combat these issues, minimum quantity lubrication (MQL) is often employed with great results. This technique creates a mist of cutting fluid and air that is sprayed onto the tool and workpiece to remove heat and provide lubrication. Its effectiveness has been demonstrated by micromilling of Nitinol, with the results showing minimal adhesions to the cutting tool, reduced flank wear, and reduced burr formation when compared to dry cutting (Weinert and Petzoldt 2006). Similar findings have also been made when compared to flood cooling (Rahman, Senthil Kumar, and Salam 2002). Figure 4 illustrates the differences in tool wear when milling using dry cutting, flood cooling, and MQL.

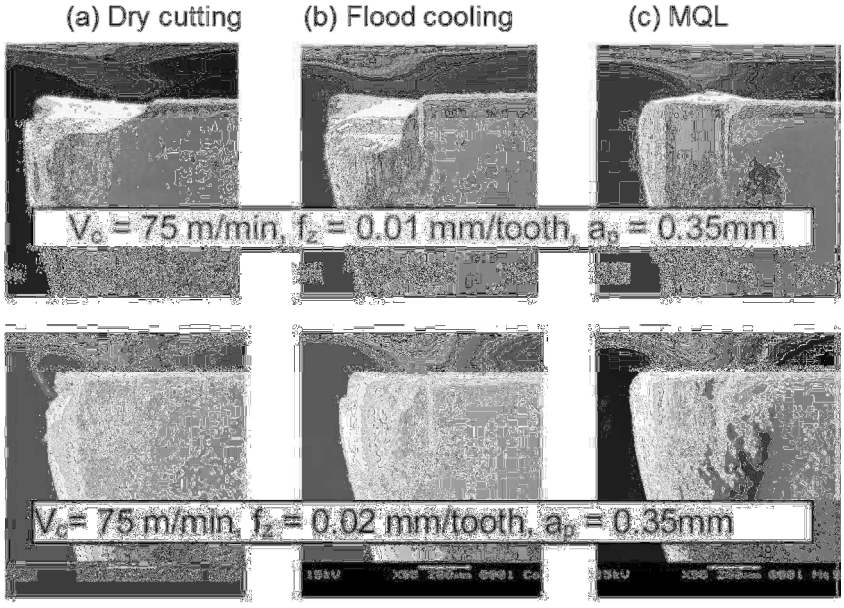

Figure 4: Tool wear comparison using dry cutting, flood cooling, and MQL (Rahman, 2002)

Additional benefits include a reduced use of the fluid itself, thus minimizing costs of purchasing new coolant and exposure of workers to chemicals that can pose a health hazard.

To determine the optimum cutting fluid, it is desired that the contact angle of a given drop be minimized to wet the greatest amount of surface area of the workpiece and tool possible (Oberg et al. 2012). The wetting properties of different coolants can be calculated by using a micropipette to dispense a drop of a known volume onto the surface of the material. This drop can be approximated as a sphere with radius R, and projected droplet diameter P, as shown in Figure 5. By measuring the value of P under a microscope, the following equation can be used to calculate the contact angle, θ:

$$\frac{P}{V^{\frac{1}{3}}} = \left[\frac{24}{\pi}\,\frac{(1 - K\cos^2\theta)^{3/2}}{2 - 3\cos\theta + \cos^3\theta}\right]^{1/3} \tag{1}$$

The value of K is determined by the angle measured, and is equal to zero for 90° < θ < 180°, and one for 0° < θ < 90°. The value of θ for varying $P/V^{1/3}$ values can then be compiled into a table or chart; using this table makes determination of the contact angle for multiple drops quite easy (Chittipolu 2009). By measuring multiple drops, an average value of the contact angle for a given cutting fluid can then be calculated.

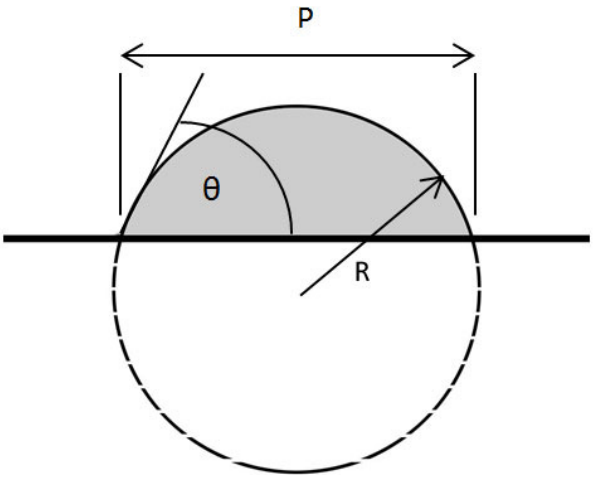

Figure 5: Drop geometry

2.2.3 Tool Coatings

A variety of coatings have been developed with the main goals of prolonging tool life and increasing cutting speeds (Stephenson and Agapiou 2006). It accomplishes these goals by:

- Providing a corrosive resistant barrier between the tool and workpiece
- Increasing wear resistance of the tool
- Decreasing friction between the tool and workpiece
- Reducing the formation of a built up edge
- Reducing plastic deformation at the cutting edge due to heating

Some factors that affect the quality of the coating include (Subramanian and Strafford 1993):

- Coating thickness
- Hardness

- Fracture toughness
- Frictional properties
- Compatibility and adhesion with the substrate
- Thermal conductivity
- Tool geometry

Tool coatings are generally applied using one of two techniques: chemical vapor deposition (CVD) and physical vapor deposition (PVD). While either process can apply multiple layers, PVD is usually applied at temperatures around 500°C, while CVD is done at approximately 1000°C (Stephenson and Agapiou 2006). This higher application temperature reduces the available tool materials that can utilize this process without degrading its mechanical properties. Studies have shown that the higher application temperature of CVD can form an eta phase between the coating and a tungsten carbide tool, reducing the transverse rupture strength by as much as 30%, and significantly weakening cutting edges (McCabe 2001).

Furthermore, PVD coatings are finer grained, allowing them to better conform to sharp cutting edges, and are typically smoother and possess better lubricity than CVD coatings. These factors make PVD coatings the ideal choice for coating precision high speed steel and tungsten carbide tools (Stephenson and Agapiou 2006). The four methods of PVD coating include low voltage electron beam evaporation, cathodic arc deposition, triode high voltage electron beam evaporation, and balanced and unbalanced magnetron sputtering (Sproul 1996) . A variety of coatings and some selected properties are shown in Table 1.

Table 1: Coating materials and important properties (Swiss-Tek Coating Inc 2010)

Coating Properties	**Cathodic Arc**									**Nano-tek**	**Nano-tek/CR**
Coating Material	TiN [1]	TiCN	TiCN-MP	TiAlCN	TiAl N	AlTiN	ZrN	CrN	CBC	AlTiN /Si_3N_4	AlCrN/ Si_3N_4
Coating Structure	Mono -layer	Gradient	Gradient	Gradient	Multi layer	Gradient	Mono-layer	Mono-layer	Gradient	Nano-compo site	Nano-compos ite
Nanohardne ss (GPa)	24	37	32	28	28	38	20	18	20	45	42
Friction (fretting) coefficient	0.55	0.2	0.2	0.3	0.6	0.7	0.4	0.3	0.15	0.45	0.35
Coating Thickness (µm)	1-5	1-4	1-4	1-4	1-4	1-3	1-4	1-4	0.5-1.5	1-4	1-5
Maximum Working Temperature	600° C	400° C	400° C	500° C	700° C	900° C	550° C	700° C	400° C	1200° C	1100° C

2.2.4 Micromachining of Nitinol

Not surprisingly, Nitinol's exceptional properties have drawn the attention of many researchers that seek to discover new methods and techniques of manufacturing products. Early research into the material discovered a strong work hardening effect that causes rapid tool wear, making the selection of proper cutting speed, feed rate, tool geometry, and cutting fluid critical (Gould 1963). It also noted that the life of carbide drilling tools was much greater than tools made of high speed steel, and that deviations of only 1.5 m/min from the optimum cutting speed (which is dependent on the specific alloy) resulted in over a 50% loss of tool life.

Further research focused on the influence of cutting speed and feed rate on drilled hole surface roughness and tool wear utilizing a 5.0 mm carbide twist drill that allowed for internal cooling supply, as well as any differences in these parameters when

comparing martensitic and austenitic alloys (Weinert et al. 2004). With cutting speeds between 80 m/min and 120 m/min, tool wear was minimal for both alloys. However, while no difference was noted in the surface roughness when drilling the martensitic alloy, a strong correlation was discovered in the austenitic alloy, with the minimum surface roughness of approximately 0.7 µm occurring at a cutting speed of 100 m/min. Utilizing cutting speeds less than or greater than this resulted in a noticeable increase in the surface roughness.

While no difference between the surface roughness was detected based on the chip load or the alloy used, it was noted that with increasing feed rate, the specific cutting energy decreased due to decreased friction, despite the increased drilling torque and feed force. This was true for both alloys; however, the martensitic alloy experienced a lower drilling torque and feed force, probably due to its lower tensile strength. It was also discovered that with low cutting speeds (approximately 5 m/min) the work hardening effect was very pronounced, extending up to 100 µm into the work piece. As the cutting speed was increased, this effect became less apparent. Similarly, increasing the feed rate creates more mechanical loads and results in more pronounced work hardening. These effects were common in both alloys, but the martensitic alloy was more affected by these issues than the austenitic alloy.

The effects of micromilling with TiAlN coated carbide tools (1 mm and 0.4 mm) were also studied (Weinert and Petzoldt 2006). When end milling with 1 mm tools, the optimal cutting parameters were a cutting depth of 100 µm, a width of cut of 250 µm, a feed per tooth of 6 µm, and a cutting speed of 47 m/min. Notably, these values were not

able to be linearly scaled down for micro tools due to a drastically reduced section modulus of the tool and the fact that rounding of the cutting edge is on the same order of magnitude as the diameter of the tool. Using the 0.4 mm end mill, the cutting depth had to be reduced to 10 μm, and the width of cut reduced to 10-40 μm to yield acceptable results.

Later research investigated the effects of drilling tool geometry and reduced diameters, specifically comparing 1.0 mm single lip drills to twist drills. Drilling with both types of tools resulted in high quality holes, but tool wear was significantly greater with the single lip drills (Biermann et al. 2010). The single lip drill has an asymmetrical cutting edge that causes radial forces to be absorbed by the guide pad. Friction between the guide pad and the hole wall creates heat that causes a "microwelding process," leading to adhesions on the drill and greatly reducing the tool life. This effect was minimized by using drills with a smaller tip angle to reduce radial forces, and also by adding a coating of TiN or TiAlN to reduce friction between the guide pad and hole wall. Due to the strong work hardening effect, cutting speeds less than 30 m/min lead to rounding of the cutting edge, and higher speeds exacerbate the adhesive wear.

Twist drills, on the other hand, showed much more promise with respect to tool life. Their symmetric geometry removes the radial force, and thus the primary source of adhesive wear. As a result, the cutting speed could be increased to 50 m/min, therefore reducing the wear due to the work hardening effect. The maximum hole depth achieved with twist drills was approximately three times that of single lip drills; with 1.0 mm diameter tools, a hole depth of 1200 mm was achieved compared to 420 mm with single

lip drills. This maximum depth attained by the 1.0 mm twist drill utilized a chip load of 5 µm, and reducing the drill diameter to 0.5 mm required a decrease of the chip load to 0.5 µm to avoid breaking the tool (Biermann et al. 2010).

2.3 Modeling

Finite element analysis has been used in previous research to analyze the dynamic behavior of microdrills to critical speeds and critical buckling loads (Gong, Ehmann, and Lin 2003). The critical speed is defined as rotational speed required to induce vibration at the resonant frequency of the drill, which can lead to premature tool failure (Azar and Samuel 2007). This critical speed can be increased with increases in the cross sectional area of the drill, which is accomplished by increasing the drill's web thickness.

Increasing the helix angle also proved to increase the critical speed of the microdrill by improving the bending stiffness. However, caution should be taken in increasing the helix angle too much, which can result in reduced chip removal, leading to increased friction and thus higher temperatures (Gong, Ehmann, and Lin 2003).

The most critical parameter influencing the critical speed was noted to be the flute length, with increasing flute length leading to a rapid decrease in the critical speed. This too had a large impact on the buckling loads, which is the required load to cause buckling sharply decreasing with increasing flute length, as would be expected by the Euler column buckling formula shown in Equation (2) (Beer et al. 2003).

$$F = \frac{\pi^2 EI}{(KL)^2} \quad (2)$$

Where:

F = critical buckling load

E = Young's modulus

I = area moment of inertia

K = support factor

L = column length

It was also noted that by increasing the drill diameter, the buckling load increased. This too is predicted by Equation (3), where the area moment of inertia of the drill can be approximated as a circle (Oberg et al. 2012):

$$I = \frac{\pi r^4}{4} \quad (3)$$

3. EXPERIMENTS

3.1 Materials

Drilling was performed on annealed Nitinol sheet of dimension 0.8 mm x 80 mm x 350 mm. The composition of this Nitinol is shown in Table 2, and selected mechanical properties are shown in Table 3.

Table 2: NiTi chemical composition from the manufacturer (Memry Corporation 2011)

Element	Percentage (wt-%)
Ni	55.49
Ti	Bal
Cr	N/A
Cu	N/A
Fe	<0.05
Nb	N/A
Co	N/A
C	310 ppm
O	185 ppm
H	3 ppm
All others	<0.05

Table 3: Mechanical properties of the NiTi sheet in as-supplied condition (Memry Corporation 2011)

UTS	1625.3 MPa
Elongation	17 %
Upper Plateau stress	148 MPa
Lower Plateau stress	N/A
Active A_f	57°C

Drilling was also completed using Aluminum 6061-T6 for verification of the FEA model. Tables 4 and 5 show the chemical composition and select mechanical properties, respectively.

Table 4: Al 6061-T6 chemical composition (Holt 1996)

Element	Percentage (wt-%)
Al	Bal
Cr	0.04-0.35
Cu	0.15-0.40
Fe	0.7
Mg	0.8-1.2
Si	0.40-0.8
Zn	0.25

Table 5: Mechanical properties of Al 6061-T6 material (Holt 1996)

Tensile Strength	310 MPa
Yield Strength	276 MPa
Elastic Modulus	68.9 GPa
Poisson's Ratio	0.33
Shear Modulus	26 GPa
Shear Strength	207 MPa
Hardness, Vickers	107

3.2. Tools and Machinery

3.2.1 Micro Drills

The majority of the experiments were completed using Performance Micro Tool's KT-0050-S standard length drills. The drills utilize a 2 flute, four-facet chisel point design, and are made from MF10 ultra-fine grade cemented carbide blanks from Mitsubishi. Some of its properties are listed in Table 6.

Table 6: Mitsubishi MF10 Carbide Properties (Mitsubishi Materials Corporation 2007)

Tungsten carbide content	92% mass
Cobalt content	8% mass
Grain size	< 0.6 µm
Hardness (HRA)	93.8
Transverse rupture strength (GPa)	4.0
Fracture toughness (MPa-$m^{1/2}$)	5.8
Density (g/cm^3)	14.6
Elastic Modulus	630 GPa
Poisson's Ratio	0.23
Shear Modulus	256.1 GPa

Each drill has a cutter diameter of 127 µm (+.0000, -7.62 µm), a flute length of 1.524 mm (± 0.1016 mm), a shank diameter of 3.175 mm (+.0000, -5.08 µm), and an overall length of 38.1 mm (± 0.127 mm). This geometry is shown in Figure 6. Verification of the FEA results was completed using drills of diameter 150 µm (+.0000, -7.62 µm), and flute lengths of 1.500, 2.500, and 3.500 mm (± 0.1016 mm).

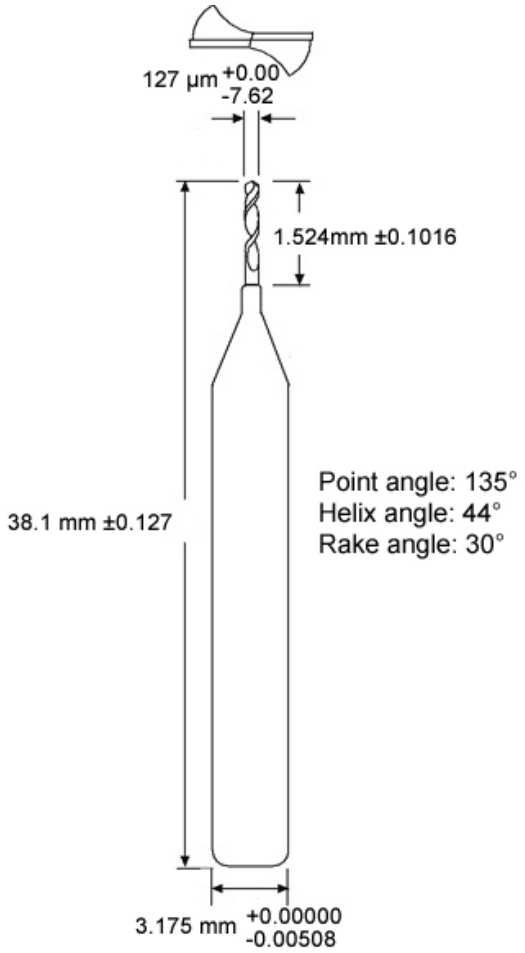

Figure 6: Drill geometry (Performance Micro Tool 2012)

Additionally, tools were tested with an AlTiN as well as proprietary Nano-tek ($AlTiN/Si_3N_4$) coatings, both provided by Swiss-Tek Coatings. Some properties of these coatings are shown in Table 1.

3.2.2 HAAS Office Mill 2

All drilling was completed using the Haas Office Mill 2 (OM-2) and its full CNC control. The OM-2 features a 50,000 RPM electric spindle rated at 270W that provides positioning accuracy of ±0.005 mm and repeatability of ±0.003 mm. The electric spindle

allows for a wide range of cutting speeds to be tested with highly accurate and repeatable results. The machine also features 19.2 m/min rapids with a maximum cutting feed rate of 12.7 m/min. Maximum travel in the X, Y, and Z axes is 305mm, 254mm, and 305mm, respectively (HAAS Automation, Inc. 2012). The workpiece was mounted in a custom made fixture to the OM-2's 5 axis trunnion rotary table.

Additional equipment installed on the HAAS OM-2 mill includes a UNIST minimum quantity lubrication system. The system is powered by a pump which was set to apply approximately 0.01 mL drops at a rate of 120 drops per minute through a nozzle that was oriented at a 60° angle to the workpiece. Air filtration was provided by a Mistbuster 850 Air Cleaner, which served to remove oil mist from the work environment.

3.2.3 Fixtures

Due to the unconventional nature of drilling in a thin sheet, a custom fixture had to be created to secure the workpiece during experiments. A small block was machined out of 6061-T6 aluminum to accept a square sheet of Nitinol cut with a GF AgieCharmilles "Cut 20 P" wire electrical discharge machine to dimensions of approximately 25 x 25 mm. A shallow pocket was milled on the HAAS OM-2 to accept the Nitinol square and ensure the bottom surface would be perpendicular to the drill. Holes were then drilled and counterbored to accommodate bolts to secure it to the machine's table.

The Nitinol square was fixed to the aluminum by the use of Loctite Super Glue, and held in place by a c-clamp for a 24 hour period to allow it to set. Though it is true

that the drill would penetrate into the fixture and glue after passing through the Nitinol sheet, any wear observed in the tool could almost be exclusively attributed to the Nitinol. Previous experiments (Mohanty 2011) have noted considerably less wear in microdrilling aluminum alloys compared with more difficult to machine metals such as titanium and stainless steel. Additionally, the ultimate shear strength of the cured Loctite Super Glue ranges from 10 to 20 MPa (Henkel Corporation 2010), which is approximately 2% of the ultimate shear strength of Nitinol.

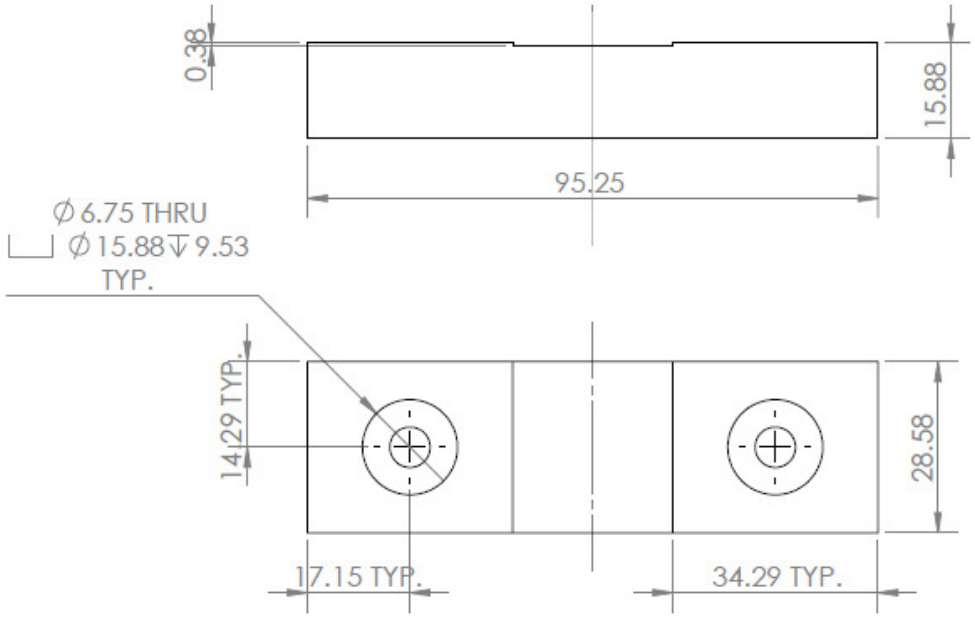

Figure 7: Test fixture used to secure the Nitinol sheet (units in mm)

Furthermore, this fixture enabled grinding and polishing the surface of the Nitinol sheet, which proved to be of critical importance in reducing drill wandering. Details of this procedure can be found in section 3.4.3.

3.3 Metrology

3.3.1 Metason 200 Ultrasonic Cleaner

This ultrasonic cleaner was used to remove oil and debris from the tools and workpieces for observation under a microscope. Isopropyl alcohol was used as the cleaning solvent. The cleaner works by producing high frequency sound waves within the solvent, which create cavitation bubbles that remove the debris.

3.3.2 Olympus STM 6 Microscope

The optical microscope was used to view and photograph the tools and workpieces in all experiments. The microscope was equipped with 4 objective lenses ranging from 1.25X to 50X, and was used in conjunction with a DP70 12.5 megapixel camera that was connected to a computer. Its ImagePro software allowed for capturing the photographs and "stitching" them together to adjust for depth of field when using higher power lenses. This composite image could then be measured with included metrology software capable of 0.1μm resolution.

3.3.4 JEOL JSM-6400 Scanning Electron Microscope

When sufficient detail of the tools' wear and BUE could not be observed using the Olympus microscope, a scanning electron microscope was employed. Capable of magnification from 10 – 300,000X with a resolution of 3.5nm, the scanning electron microscope allowed for much easier recognition of wear and built up edge formation on the tool. The microscope was also equipped with an energy dispersive x-ray apparatus, which enables the user to easily distinguish between the tool and any workpiece material that remained after drilling.

3.3.5 Keyence LK-G 1577 Laser Displacement Sensor

The laser displacement sensor was critical to determine the Z-axis offset for the micro drills. Incorrect offset could result in tool fracture if set too low, or improper hole depth if set too high. To set the proper offset, a foam block was affixed to a bar of aluminum that was ground flat. This foam block had a mark on the center that the laser focused upon, and when the sponge was removed from the laser, the height of the foam-aluminum assembly could be precisely determined within ± 0.02%. This height was regularly checked to ensure that any deformation of the sponge was accounted for. With an average experimental height of 30.165mm, the maximum measurement error was approximately ± 6 microns. The tool could then be touched to the foam without fracturing, and the height of the foam block subtracted from the offset to accurately zero the drill.

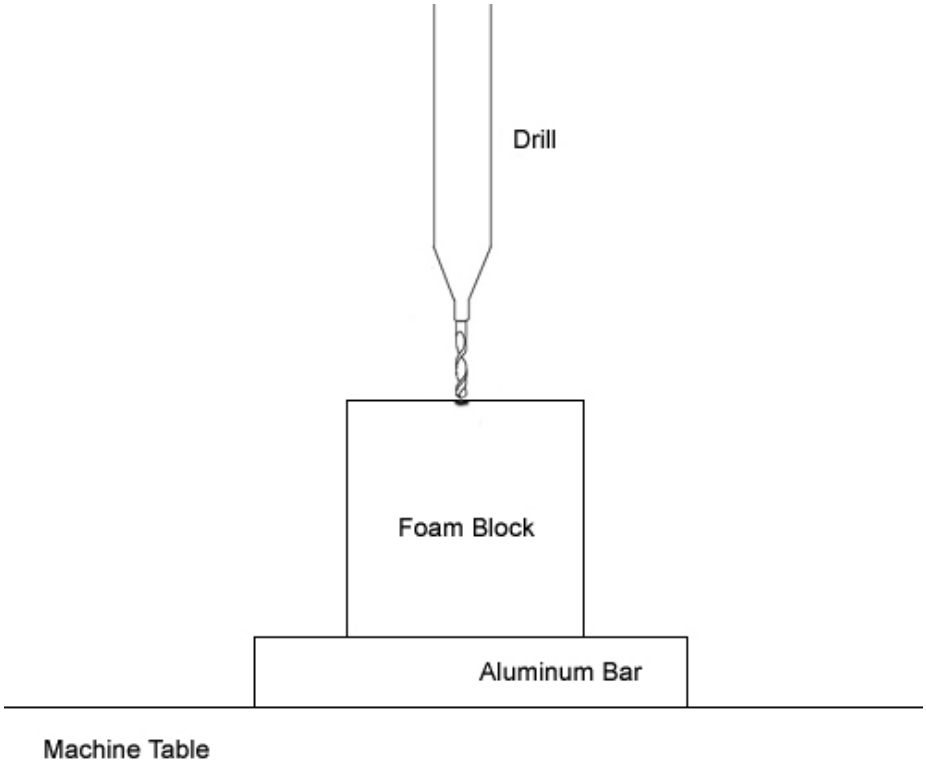

Figure 8: Foam block mounted on an aluminum bar used to set the Z-axis offset

3.3.6 Leco LM300AT Microhardness Tester

Microhardness measurements were taken of the uncoated tungsten carbide blanks for comparison with the Nano-tek and AlTiN coatings. The LM300AT allows for loads between 1-2000 gf to be applied to the workpiece, and features objective lenses from 2.5X to 100X to enable accurate measurements of the Vickers pyramid indention. Due to the depth of the indentation, this method of testing proved unreliable for measuring the hardness of the thin coatings.

3.3.7 Hysitron TI 900 TriboIndenter

Nanoindentation testing was performed to characterize the Nano-tek and AlTiN coatings used in the experiments. The TI 900 TriboIndenter features load resolution of less than 1 nN as well as Z axis travel resolution of 3 nm, making it ideal for measuring the Young's modulus and hardness of very thin coatings.

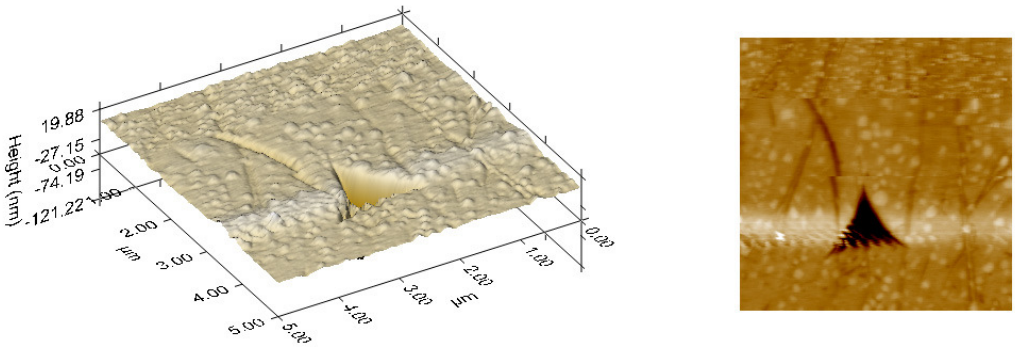

Figure 9: Example of a nanoindentation on quartz

3.4 Procedure

3.4.1 Contact Angle

In order to maximize the potential of the minimum quantity lubrication system, the proper cutting fluid must be used. Thus, it was necessary to perform experiments on the uncoated tungsten carbide, AlTiN and Nano-Tek coatings, and the Nitinol itself. To test the coatings and tungsten carbide, blanks supplied by PMT and coated by Swiss-Tek were used. These experiments followed the procedure outlined in section 2.2.2. Three oil

based lubricants – Coolube 2210, 2210EP, 2200, and 2300HD, and one water soluble lubricant – Rustlick 1:15, were studied.

Using a Socorex Acura 825 adjustable volume micropipette, a drop of 0.25μL was carefully placed on a flat test specimen sitting on the Olympus STM 6 microscope. A photograph was then immediately taken before the drop evaporated. Eight drops were placed on each blank with a single cutting fluid. When all drops has been placed and photographed, the micropipette and test material was cleaned in the ultrasonic cleaner to prepare it for experiments with a different cutting fluid. This process was repeated until all five lubricants were tested on each material blank.

3.4.2 Hardness Testing

In order to characterize the hardness of the Nano-tek and AlTiN coatings, nanoindentation tests were carried out using the Hysitron TI 900 TriboIndenter. A 10050 μN load was placed on the same blanks used for the contact angle measurements using a Berkovich indenter tip for a period of 23 seconds. Nine indentions were created on four AlTiN and Nano-tek coated tungsten carbide blanks, and their respective hardness measurements recorded and averaged.

Similar experiments were carried out with the Leco LM300AT microhardness tester to measure the hardness of the uncoated tungsten carbide blanks. A 1 kgf load was placed the blanks for a period of 13 seconds using a Vickers microindenter. Eight indentions were created and the results compiled.

3.4.3 Workpiece Surface Preparation

Before drilling could begin, it was necessary to polish the surface of the Nitinol sheet. Failure to do so could result in excessive tool wandering which may lead to failure (Mohanty 2011). Using the fixture described in Section 3.2.3, the Nitinol sheet was subjected to grinding starting with 100 grit sandpaper, and progressively increased to 600 grit. The sheet was then polished on a flat metallographic polishing wheel with abrasive Al_2O_3 particles of 0.5 μm, resulting in a mirror finish.

3.4.4 Microdrilling

Prior to the actual experimentation, each drill was cleaned in the ultrasonic cleaner for five minutes, and then dried with compressed air. Next, the tool was observed under the microscope for any obvious flaws. While under the microscope, photographs were taken of each cutting edge so that its wear could be documented after drilling. Grinding marks or other distinguishing features were used to differentiate between one cutting edge and the other.

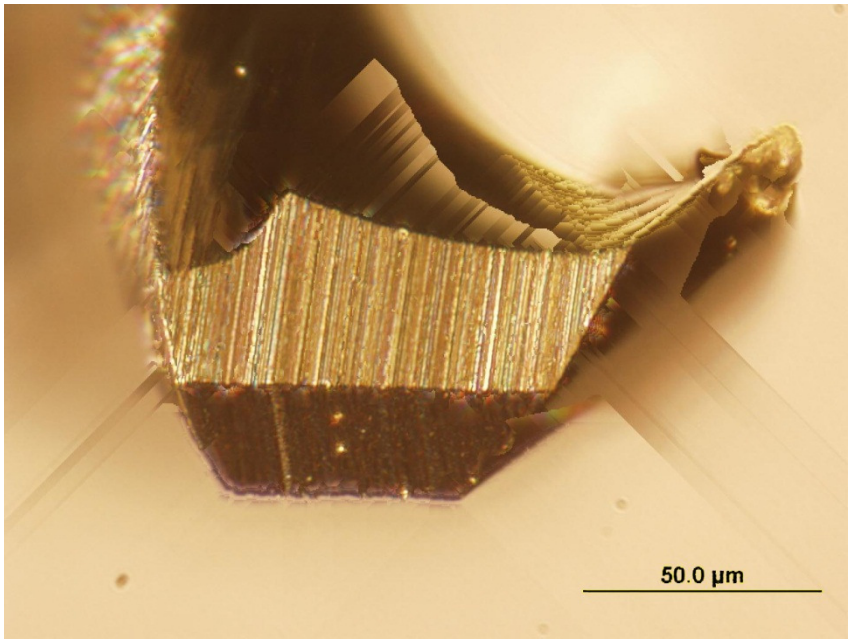

Figure 10: Optical image of a new, uncoated Ø127 µm WC microdrill

With the tool ready for the experiment, it was returned to its storage box in a numbered slot to allow for easy identification in the future. The HAAS OM-2 was next turned on and a warm up program run. This program, along with all the G-code used throughout these experiments, is shown in Appendix A. A dial indicator with a magnetic base was attached to the spindle head and used to verify the perpendicularity of the drill and workpiece to ±0.025 mm, less than a fifth of the diameter of the drill. Once the machine was ready, the tool was carefully placed in the collet and tightened with two wrenches, and the X, Y, and Z offsets were determined. The X and Y offsets were set to a location on the sheet where a row of 10 holes could be drilled, and the Z offset was determined using the procedure outlined in section 3.3.6.

Next, the UNIST mist nozzle was aligned at approximately 60° and 25mm away from the drill tip, and was mounted on the spindle such that it would maintain this orientation during machining. The pump was turned on and allowed to run for one minute to ensure that a steady stream of micro mist was established. Drilling proceeded by following a CNC program that utilized a peck cycle in a subroutine. This subroutine could be called out to drill 10 holes in a row with a pitch of 0.254mm, or simply twice the drill diameter. Total drill depth was set to 0.9mm to guarantee that all holes fully penetrated the nominal 0.8mm thick sheet of Nitinol. The pecking cycle followed the following equations (Hung 2012):

$$\frac{P}{D} = \frac{1}{9(-1.5R + 19.5)} \quad for\ R \leq 10 \tag{4}$$

$$\frac{P}{D} = 0.5 \quad for\ R > 10 \tag{5}$$

Where:
P = incremental pecking depth (mm)

D = drill diameter (mm)

R = intermediate drill aspect ratio (hole depth / drill diameter)

Thus, the full pecking cycle used can be summarized in Table 7:

Table 7: Pecking cycle for a Ø127 μm drill

Peck number	Hole depth (mm)	Aspect ratio	P/D	Pecking depth (mm)
1	0.254	2	1.83	0.254
2	0.487	3.83	1.53	0.233
3	0.649	5.36	1.27	0.162
4	0.781	6.63	1.06	0.132
5	0.900	7.70	0.88	0.119

This pecking cycle was critical in that it allows for the cutting fluid to cool the tool and flush chips away. As the hole gets deeper, it is more difficult for the tool to be wetted by the lubricant, so the pecking depth must be decreased to avoid overheating and chip clogging.

3.4.5 Tool Wear Measurements

Upon completion of every 10^{th} hole, the tool was removed from the collet and taken to the laboratory for ultrasonic cleaning and examination under the optical microscope. Photographs were taken and then superimposed over the photos of the brand new tool for wear measurement. The ground edge marked in Figure 11 was used as a reference line for each measurement. Next, a reading was taken from the outermost point of the cutting edge, which is indicated as the measurement line. This point was chosen to be representative of tool wear because it was the point that experienced the highest cutting speeds due to its distance from the axis of rotation. Accordingly, it was the point that would experience the most rapid rate of wear.

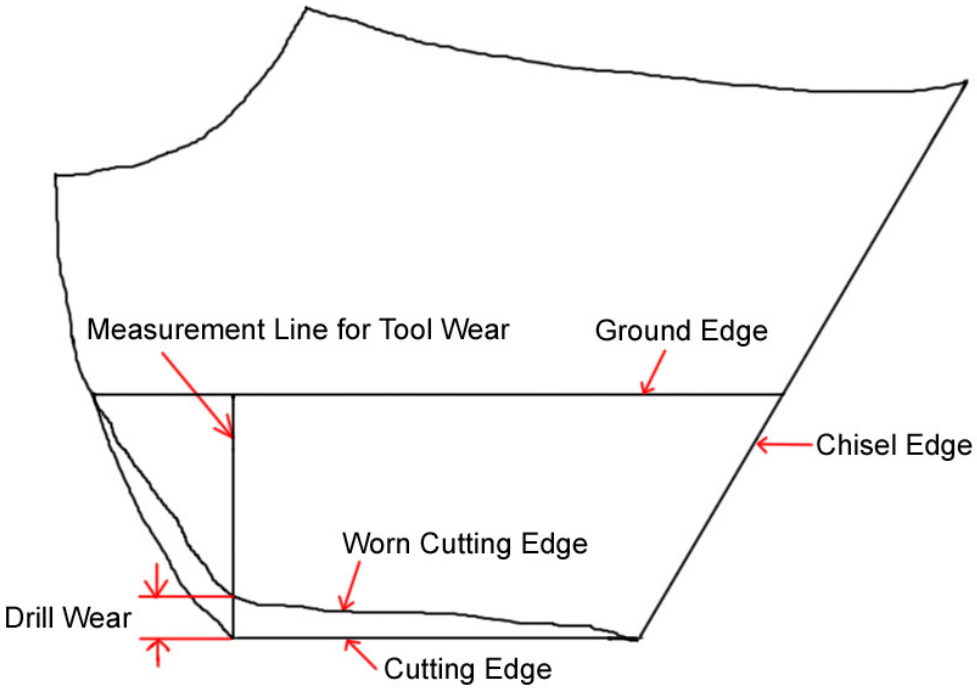

Figure 11: Measurement of tool wear

When all documentation had been made, the tool was returned to the machine collet and the Y offset reduced by 0.5mm to start another row of 10 holes. This process was repeated until either the tool fractured or was too worn to continue. A list of all cutting conditions and tools used for the experiment is compiled in Table 8. The chip load for all tools in this table was 0.02 μm per tooth. This factorial experiment design utilized spindle speeds from 8,000 to 50,000 RPM to test the tools' response over a wide range of cutting speeds.

Table 8: Cutting conditions for Ø127 µm WC drill, chip load 0.02 µm/tooth

Tool Number	Coating	Spindle Speed (RPM)	Cutting Speed (m/min)	Feed Rate (mm/min)
1	Uncoated	35,000	13.96	1.4
2	Uncoated	15,000	5.98	0.6
3	Uncoated	50,000	19.95	2.0
4	Uncoated	8,000	3.19	0.32
5	AlTiN	15,000	5.98	0.6
6	Nano-tek	35,000	13.96	1.4
7	Nano-tek	8,000	3.19	0.32
8	AlTiN	8,000	3.19	0.32
9	AlTiN	35,000	13.96	1.4
10	Nano-tek	15,000	5.98	0.6
11	Uncoated	15,000	5.98	0.6
12	Nano-tek	50,000	19.95	2.0
13	Uncoated	35,000	13.96	1.4
14	Uncoated	50,000	19.95	2.0
15	Uncoated	15,000	5.98	0.6

3.4.6 Built Up Edge Etching

When all drilling was completed with a tool, a built up edge had formed along the chisel and cutting edges. To remove this built up edge for photographing under the scanning electron microscope, a solution of HF:HNO_3:H_2O mixed to a 1:5:20 ratio was used to achieve a material removal rate of 0.1 µm/s (Chen and Wu 1999). A fixture, made out of PTFE so as to be non-reactive with the acids, was machined to hold three tools at once. This fixture was placed in a beaker containing the chemical solution and set in an ultrasonic cleaner to agitate it for 3 minutes. The tools were then carefully removed from the fixture and rinsed with water to neutralize the acid. This aggressive technique unfortunately etched the carbide as well, and no further drilling was completed after etching.

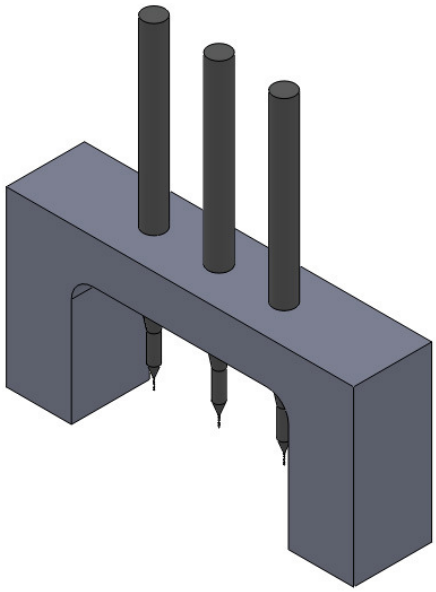

Figure 12: Chemical etching fixture

3.4.7 Hole Positioning Measurements

In addition to tool wear, measurements were also made to study the positional accuracy of the drilled holes for the tools in Table 8. When drilling had been completed, the workpiece was removed from the vise and cleaned ultrasonically. High resolution photographs were then taken of each hole and stitched together into one image.

To determine a baseline for positional measurements, the center of the first, fifth, and tenth holes were measured. These holes were chosen under the assumption that positional accuracy would be greatest in the early stages of the tool's life before it has experienced significant wear. The photo of the entire hole map was then rotated by the average of the angular difference between the first hole and the fifth, and the first hole and the tenth. Rotating the image was necessary to account for any angular

misalignment between the photos and the actual movement of the X and Y axes of the OM-2. Horizontal and vertical lines were then drawn on the map using SolidWorks at the nominal distance between holes: 0.254 mm in the horizontal, and 0.5 mm in the vertical. From here, the distance of each hole's center to its nominal location could be measured. Thus, the positional accuracy as a function of the tool's coating, cutting parameters, and depth drilled could be obtained.

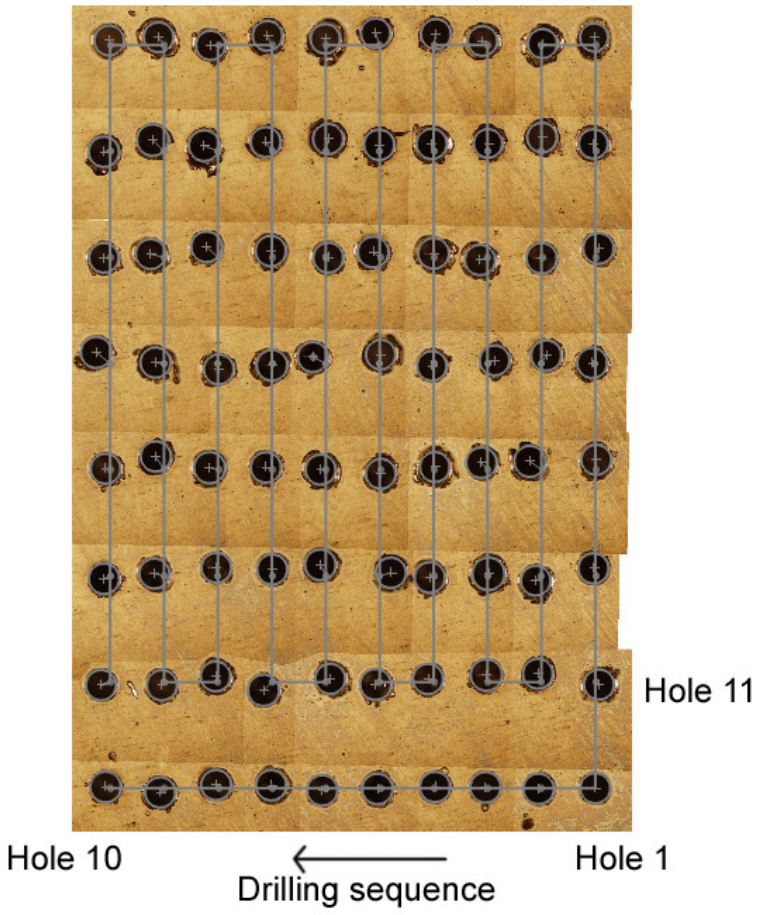

Figure 13: Typical hole map with measuring lines (Vc=3.2 m/min, uncoated tool, Nitinol)

3.4.8 Hole Diameter Measurements

With a map of the holes for each tool already created, measurements could easily be taken of the diameter of the holes to understand the correlation between the tools' coating, cutting conditions, drill depth, and the variance in hole diameter. Three measurements of the diameter of every fifth hole were taken using SolidWorks. The measurements were taken by drawing a three point perimeter circle around the hole and calibrating to the scale shown in each photo. Multiple measurements were taken to account for uncertainty in measuring the true diameter of the hole, which can be difficult to determine due to the presence of burrs. The average of these measurements and their standard deviation was taken and compiled.

3.4.9 Finite Element Modeling

First, a model of the tool geometry was constructed using SolidWorks. The model was based on carbide tools provided by Performance Micro Tool with a diameter of 0.15mm, and flute lengths varying from 1.5mm, 2.5mm, and 3.5mm. The flute length of the model was scaled up to match the dimensions of these studies. Additional models were created with a diameter of 0.2mm and flute length of 1.5mm, and a diameter of 1.0mm and flute length of 1.5mm to compare the model with published data.

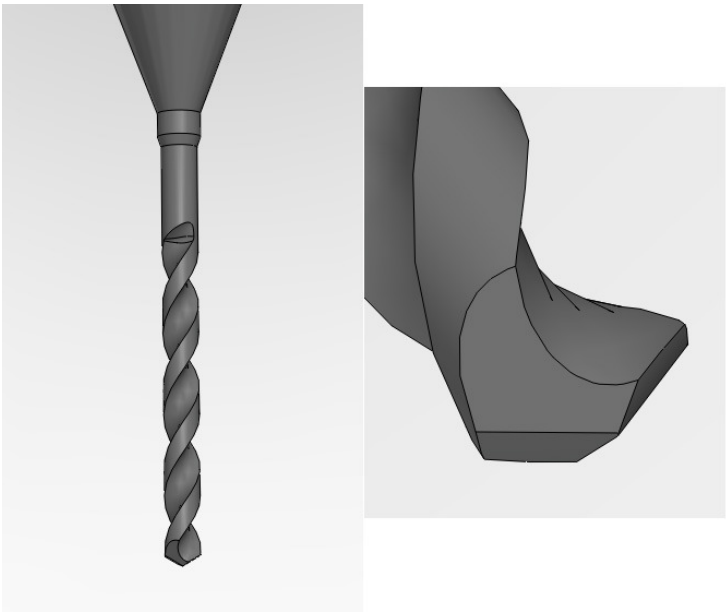

Figure 14: Drill model geometry

These tools were subjected to a process that began with drilling two holes using the pecking cycle outlined in section 3.4.3 with a chip load of 0.02µm. Upon successful completion of these holes, the chip load was increased and an additional two holes were drilled. This was repeated until failure occurred. Experiments were conducted with spindle speeds of 8,000, 15,000, and 35,000 RPM.

Finite element analysis was completed using the SolidWorks Simulation package. The software utilizes quadratic, 10 node tetrahedral elements to create the mesh used for analysis (Dassault Systemes 2012).

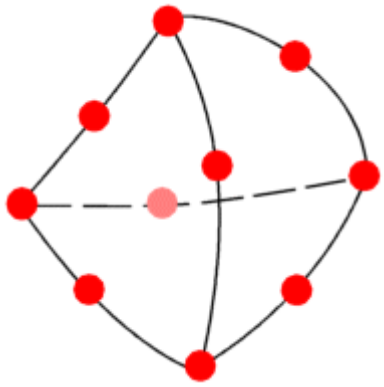

Figure 15: Ten node quadratic tetrahedral element used for finite element analysis (Dassault Systemes 2012)

Elements of decreasing size were used to verify convergence of the solution. The average element sizes are shown in Table 9 and illustrated on a 0.2 mm drill in Figure 16. All data reported is from the 0.0127 mm elements.

Table 9: Average element sizes used for meshing

Element Size
.0508 mm
.0254 mm
.0127 mm

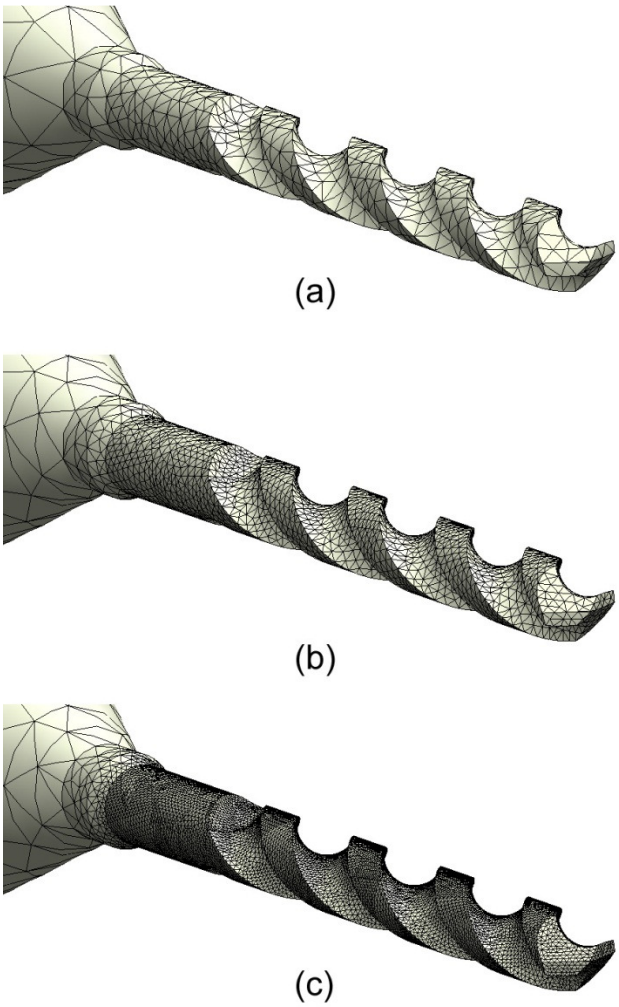

Figure 16: Element size comparison for a meshed Ø0.2mm drill. Average element size of (a) 0.0508 mm, (b) 0.0254 mm, and (c) 0.0127 mm.

4. RESULTS AND DISCUSSION

4.1 Contact Angle

Data compiled from the analysis of the cutting fluid was crucial to determining the ideal lubricant for use in proceeding microdrilling experiments. The first material tested was the uncoated tungsten carbide blank. Data regarding the inaccuracy and imprecision of the micropipette is tabulated in Table 10. With a nominal drop size of 0.25μL, the volume measurements fall into the "minimum volume" category.

Table 10: Micropipette inaccuracy and imprecision data (Socorex Isba S.A 2012)

Inaccuracy			
Volume	Minimum Volume	Mid Volume	Maximum Volume
0.1-2 μL	< ±6.0%	< ±4.0%	< ±2.0%
Imprecision			
Volume	Minimum Volume	Mid Volume	Maximum Volume
0.1-2 μL	< ±5.0%	< ±3.3%	< ±1.5%

Because the drop was assumed to be a spherical shape, its diameter needed to be measured. In practice, the drops were not truly spherical, so each drop was next measured at four different diameters to determine an average diameter to be used with Equation 1 to determine the contact angle. These measurements were taken from the center of the drop in 45° angles as shown in Figure 17.

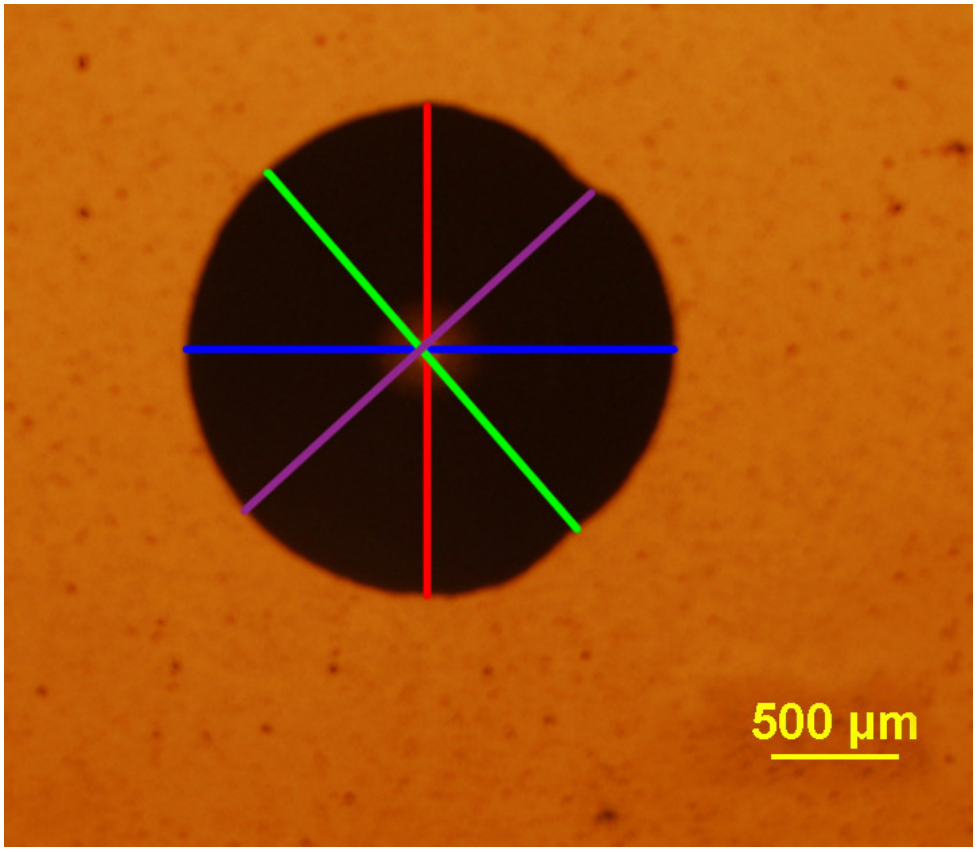

Figure 17: Drop diameter measurements, 0.25µL of CL2200 on AlTiN

Next, a table was constructed for every 0.05° increment to calculate the $\frac{P}{V^{\frac{1}{3}}}$ value required to generate that particular angle. The values determined from the experiments were then compared to this table to evaluate its contact angle.

Results from the study are shown in the following figures. Each bar in the graph represents the measurements made from one drop.

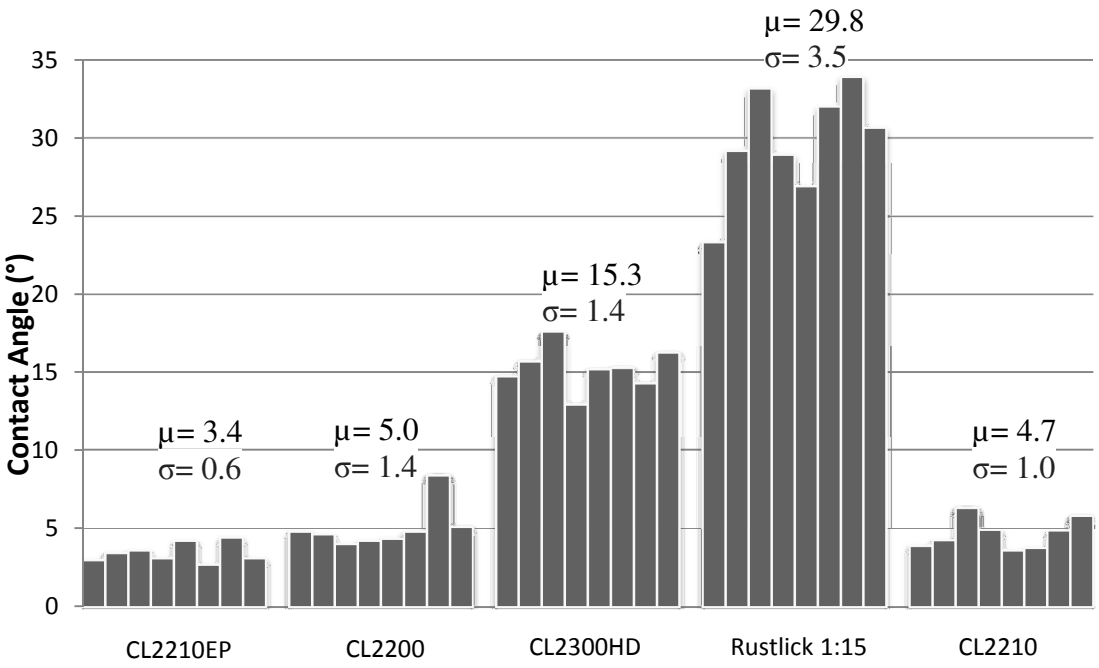

Figure 18: Contact angle for cutting fluid droplets on WC. Drop volume 0.25 μm, μ= average, σ=standard deviation.

The CL2210EP, CL2200, and CL2210 lubricants performed nearly identically with average contact angles measuring less than or equal to 5°, while CL2300HD and Rustlick measured approximately 15° and 30°, respectively. Results from this study were perhaps the most critical, as the majority of the drilling experiments were carried out with uncoated tungsten carbide tools. Thus, the CL2210EP showed itself to be the optimal choice for minimizing the contact angle.

Next, the AlTiN coating was tested. Results indicate a clear benefit in surface wetting ability when using CL2210 as opposed to the CL2210EP that was optimal for uncoated tungsten carbide. The average contact angle with CL2210 at 7.1° was less than half that of CL2210EP at 15.9°. Interestingly, the Rustlick and CL2300HD lubricants

showed nearly identical contact angles, in stark contrast to their angles displayed with the uncoated tungsten carbide.

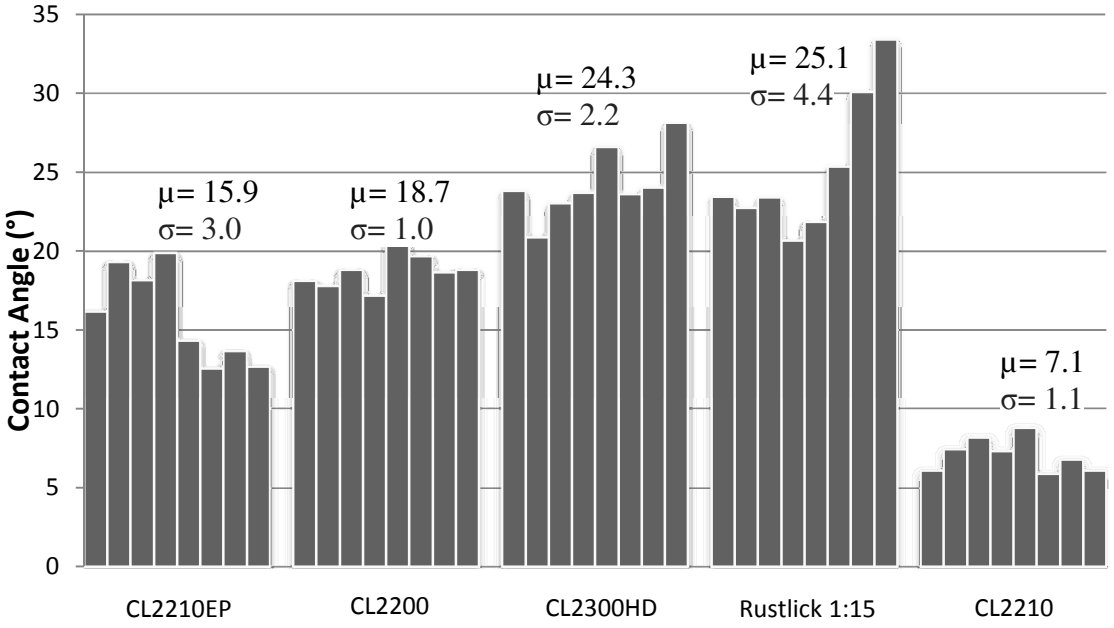

Figure 19: Contact angle for cutting fluid droplets on AlTiN. Drop volume 0.25 μm, μ= average, σ=standard deviation.

The Nano-Tek coating showed very similar results to the AlTiN coating, with the CL2210 again providing the best surface wetting by being the only lubricant that provided a contact angle of less than 10°.

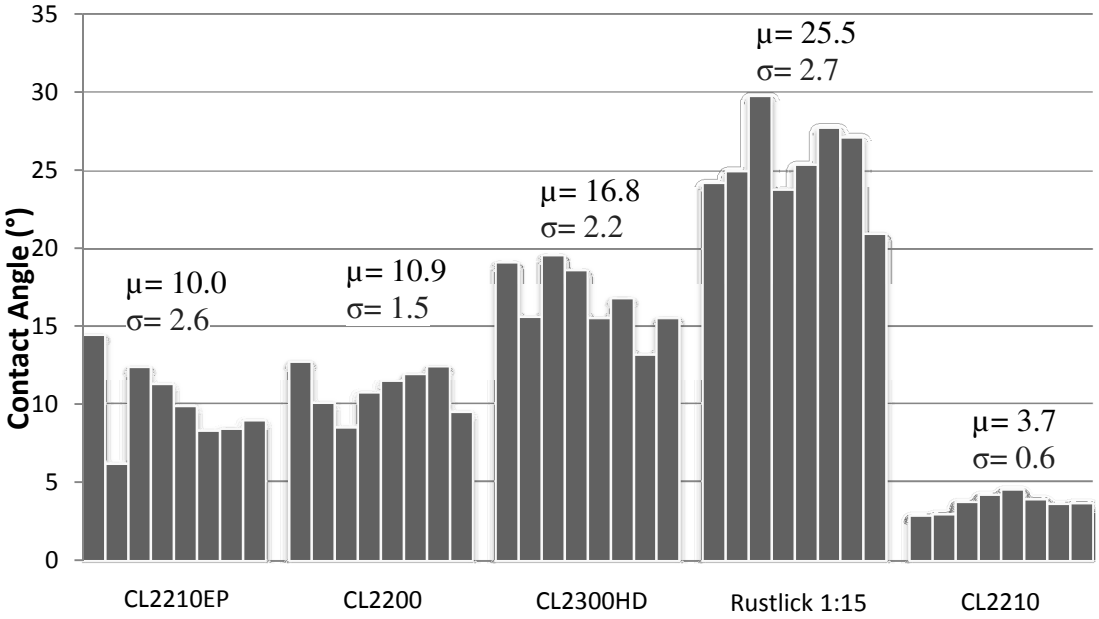

Figure 20: Contact angle for cutting fluid droplets on Nano-tek. Drop volume 0.25 μm, μ= average, σ=standard deviation.

Lastly, the lubricants were measured on a sheet of Nitinol that would later be used for drilling. Surface wetting on the workpiece material was critical to reducing friction, and thus reducing temperatures, which in turn could lead to early tool failure and an increased formation of a built up edge.

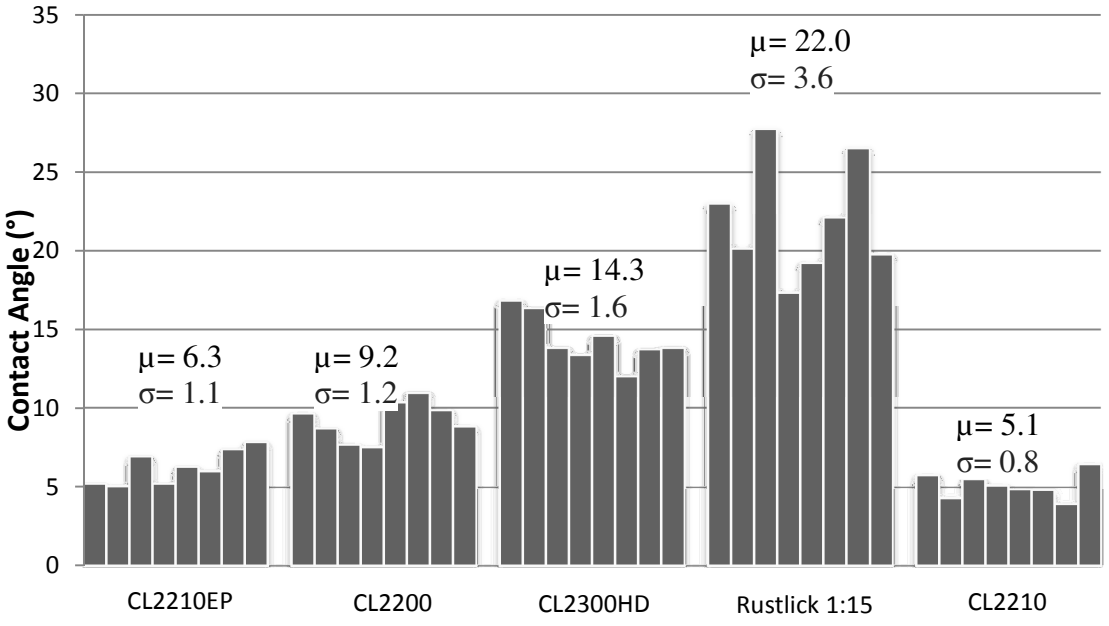

Figure 21: Contact angle for cutting fluid droplets on NiTi. Drop volume 0.25 μm, μ= average, σ=standard deviation.

Again, similar results to the previous experiments were noted, with the CL2210 cutting fluid producing the lowest average contact angle closely followed by CL2210EP. The superiority of the CL2210 is clearly demonstrated when compared to the water soluble Rustlick lubricant as shown in Figure 22. Based on the results of these experiments, CL2210 was chosen for all drilling operations, as it provided the maximum surface wetting for all cases except for the uncoated tungsten carbide, where it was nearly equal to the better performing CL2210EP.

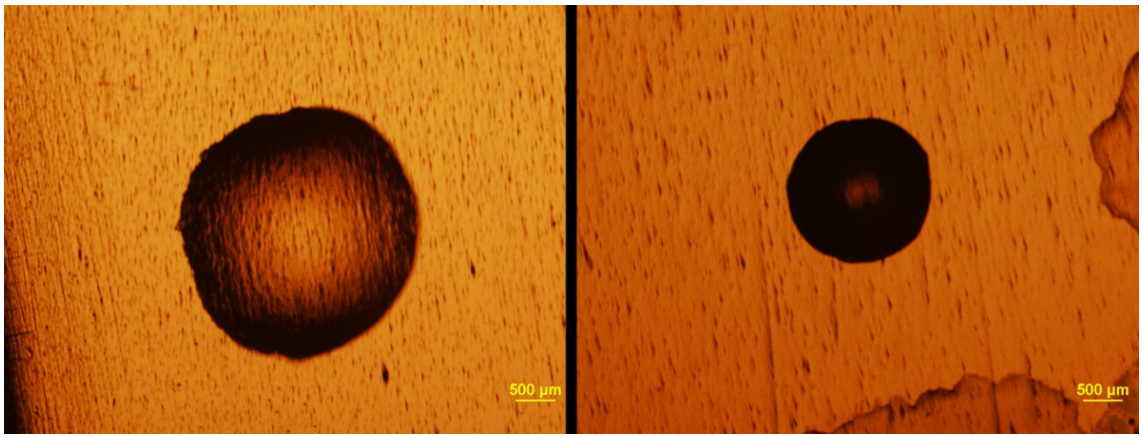

Figure 22: Wetting of CL2210 (left) and Rustlick (right) on NiTi, 0.25µL

4.2 Coating Analysis

Due to the thin coating of the Nano-tek and AlTiN specimens, a direct measurement of the Vickers hardness using the Leco LM300AT microhardness tester was not possible. The larger size of its indenter penetrated through the coating and into the substrate, giving unreliable results. Although the hardness from the nanoindenter tests was recorded in GPa, a direct comparison to the Vickers scale can be made (Nanomechanics 2013) using Equation (6):

$$HV = 94.5H \tag{6}$$

Where:

HV = Vickers hardness

H = Nanoindentation hardness (GPa)

An increase in hardness of about 56% for the Nano-tek coating and 36% for the AlTiN coating provides a substantial increase in wear resistance compared to the uncoated tungsten carbide. The results are shown in Figure 23 and Table 11.

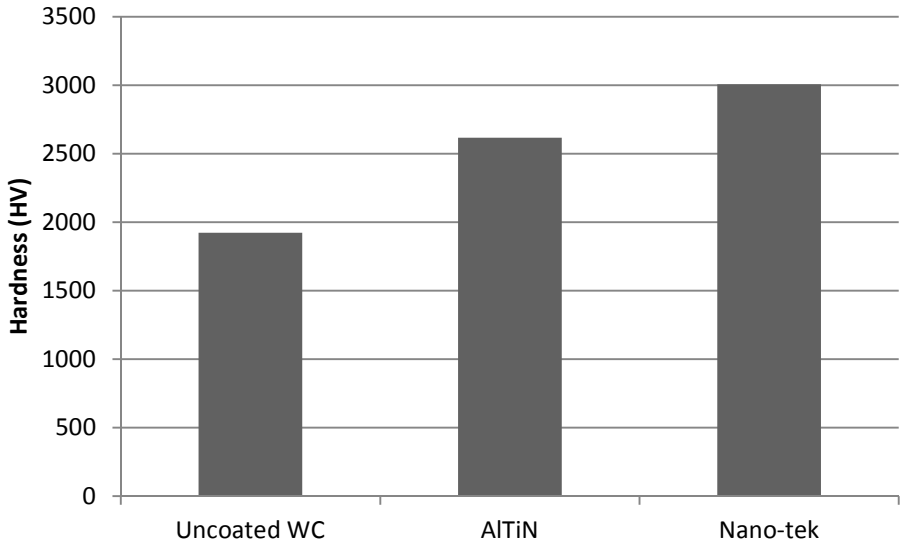

Figure 23: Vickers hardness of coated and uncoated WC blanks

Table 11: Vickers hardness measurements

	Uncoated WC	AlTiN	Nano-tek
Average hardness (HV)	1923.4	2615.5	3005.9
Median hardness (HV)	1916.3	2614.7	2771.3
Standard deviation	41.0	177.8	929.4
Percent increase in hardness above uncoated WC	-	36.0	56.3

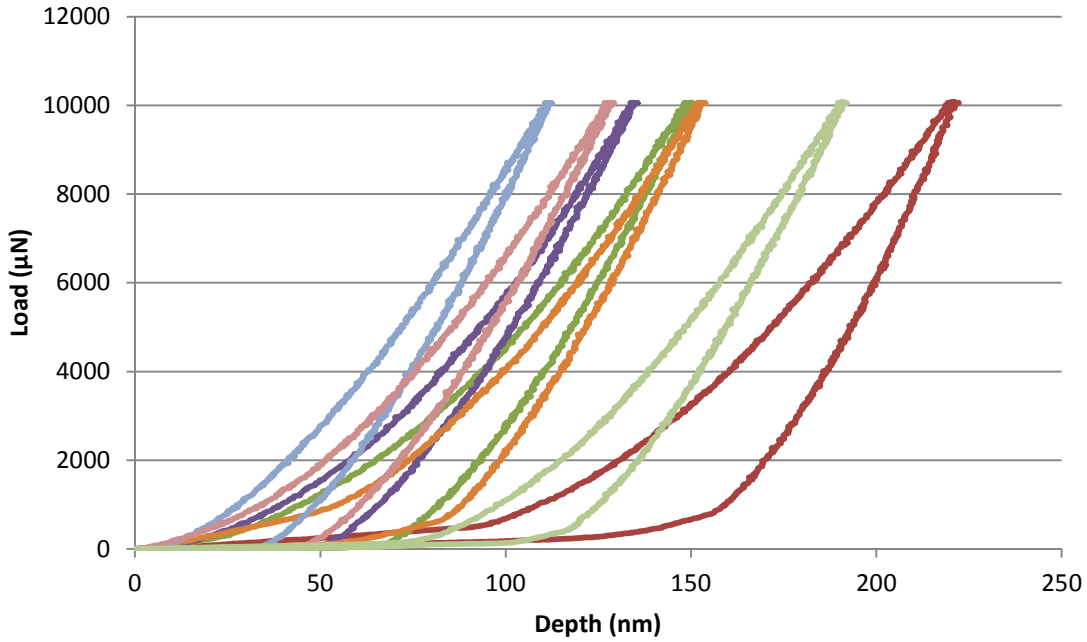

Figure 24: Load versus depth measurements of the nanoindenter. Eight indentations in a Nano-tek coated WC specimen

The nanoindentation testing was also able to provide the elastic modulus of the two coatings:

Table 12: Elastic modulus measurements of Nano-tek and AlTiN coatings

	Nano-tek	AlTiN
Average elastic modulus (GPa)	283.3	254.3
Median elastic modulus (GPa)	277.4	253.3
Standard Deviation	48.7	13.3

The standard deviation of both the hardness and elastic modulus of the Nano-tek coating is considerably larger than that of the AlTiN coating and uncoated tungsten carbide, indicating greater non-uniformity in its application to the substrate.

Measurements of the Nano-tek coating thickness were also performed using a Calotest. This method utilizes a rotating ball and abrasive fluid to indent a spherical depression into the coating and substrate. The indentation can then be examined under a microscope to calculate the thickness based on measurements of *X* and *Y* (see Figure 25) and the following equation (PVD Coatings 2013):

$$t = \frac{X * Y}{D} \tag{7}$$

Where:

t= coating thickness

X, Y = geometric measurements of the indentation

D = diameter of the spherical indenter

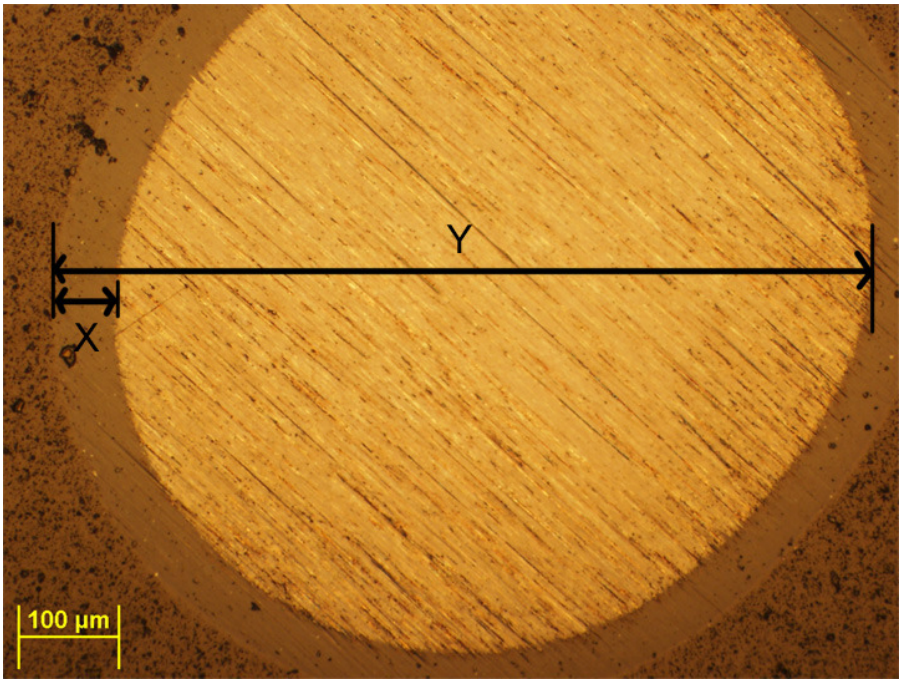

Figure 25: Calotest indentation in Nano-tek coated WC specimen

Using this method, the results of eight separate indentations yielded an average thickness of 1.831 µm with a standard deviation of 0.147 µm. The indentations were then measured using a laser interferometer (Figure 26) to confirm the results, with an average thickness measured of 1.832 µm and a standard deviation of 0.096 µm.

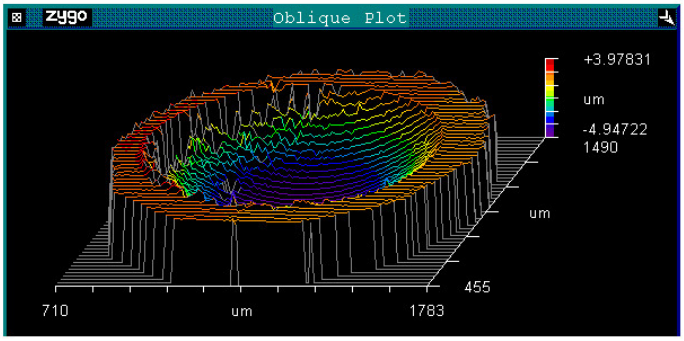

(a)

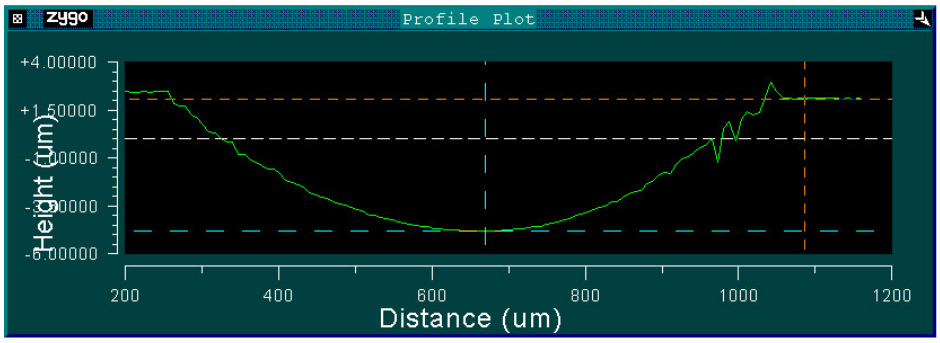

(b)

Figure 26: Oblique plot (a) and profile plot (b) of a Calotest indentation using a laser interferometer

Finally, these observations were confirmed when the Nano-tek coated tools were examined under the SEM. The peeling of the coating shown in Figure 27 reveals a thickness of approximately 2 μm.

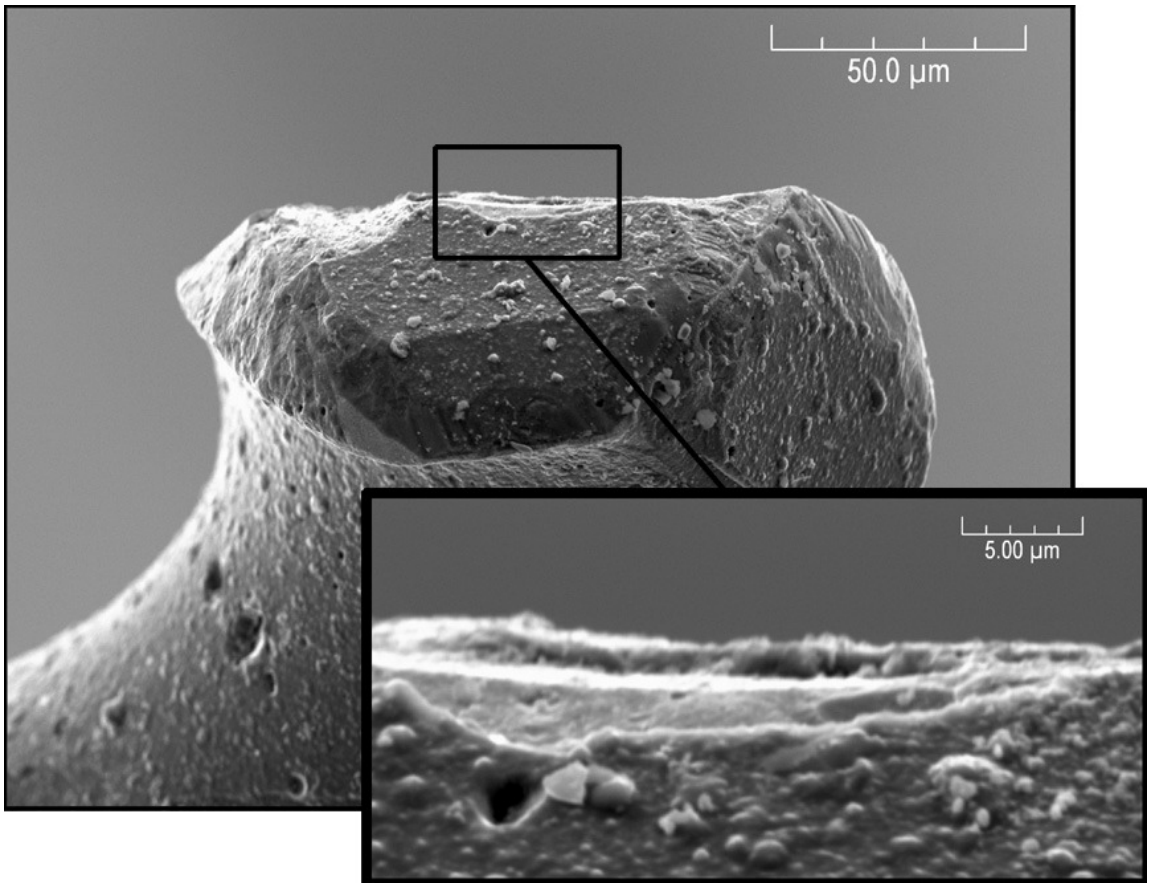

Figure 27: Peeling of the Nano-tek coating. Etched after drilling 32mm on Nitinol at Vc=6.0 m/min, 0.02 µm chip load, with CL2210 micromist

4.3 Tool Wear

Tools 1 through 3 in Table 8 were used to gain experience with drilling in NiTi, and two key observations were made. First, it became clear that it was necessary to polish the NiTi sheet (see Figure 28) prior to drilling to reduce wandering of the drill. This was also discovered when microdrilling stainless steel and aluminum (Mohanty 2011). Second, it was learned that using a chip load of 0.02µm allowed for holes to be drilled without breaking the tools. It was important to obtain this value because no prior

research had utilized tools as small as 127 µm, and cutting conditions do not scale down linearly with tool diameter (Weinert and Petzoldt 2006). This provided a chip load that could be maintained constant while other cutting parameters were modified to study their effect on the cutting process.

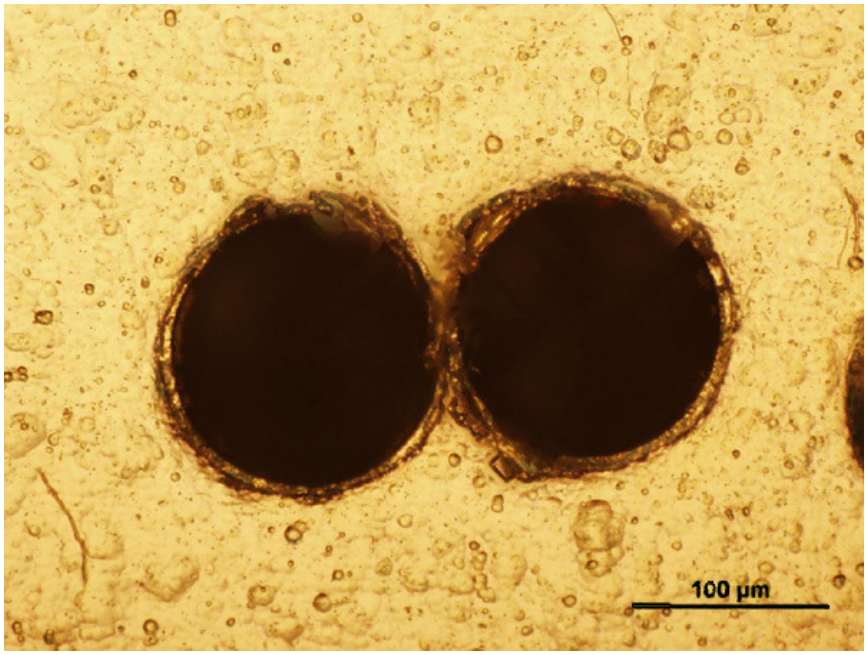

Figure 28: Extensive drill wandering on unpolished NiTi (uncoated Ø127 µm WC drill, Vc=14.0 m/min, 0.02 µm chip load, with CL2210 micromist)

4.3.1 Uncoated Tools

As expected, the location showing the most wear for all tools was on the outermost portion of the cutting edge. This wear can be approximated by a logarithmic curve when measured against distance drilled (Mohanty 2011). This plot demonstrates the average tool wear measured on both cutting edges. At the maximum spindle speed of 50,000 rpm and cutting speed of 20 m/min for a 127 µm diameter tool, the uncoated tool

experienced severe abrasive wear along the entire length of the cutting edge as well as the formation of a large built up edge on the chisel edge. After drilling to a depth of only 8.0 mm, the cutting edge was completely worn (see Figure 29). The cutting speed of 20 m/min was less than half the optimum cutting speed of 50 m/min discovered in previous research using 1.0 mm diameter TiAlN coated carbide tools, (Biermann et al. 2010) yet it proved to be impracticably high for tools almost one tenth its diameter.

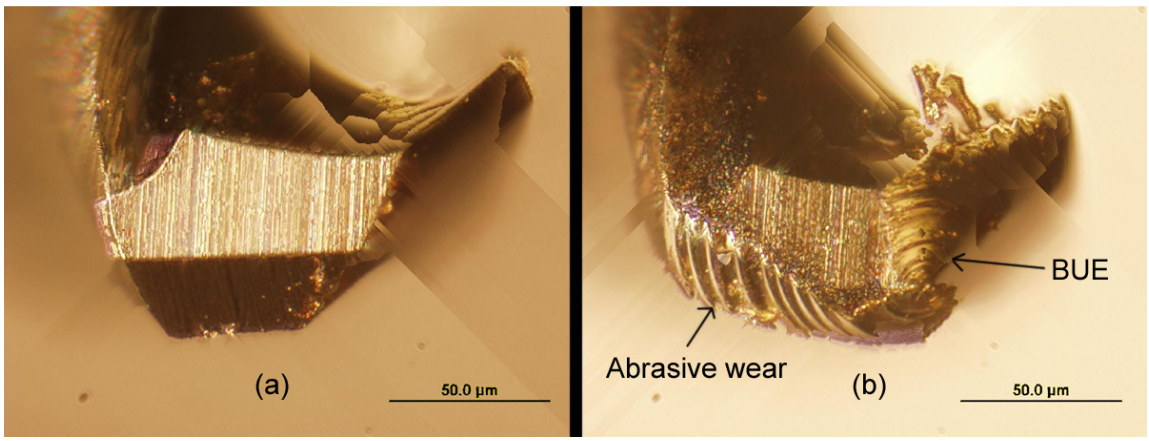

Figure 29: Wear of an uncoated WC Ø127 µm microdrill. (a) New tool and (b) significant abrasive wear after drilling 10 holes (8.0mm) on Nitinol. Vc=20.0 m/min, 0.02 µm chip load, with CL2210 micromist.

At the opposite extreme value of cutting speeds tested during the experiments, tool wear was considerably less when holes were drilled at a speed of 3.2 m/min. Built up edge formation was relatively light on the cutting edge, but extreme on the chisel edge as a result of decreasing cutting speeds near the central axis of the tool, where the cutting speed is zero.

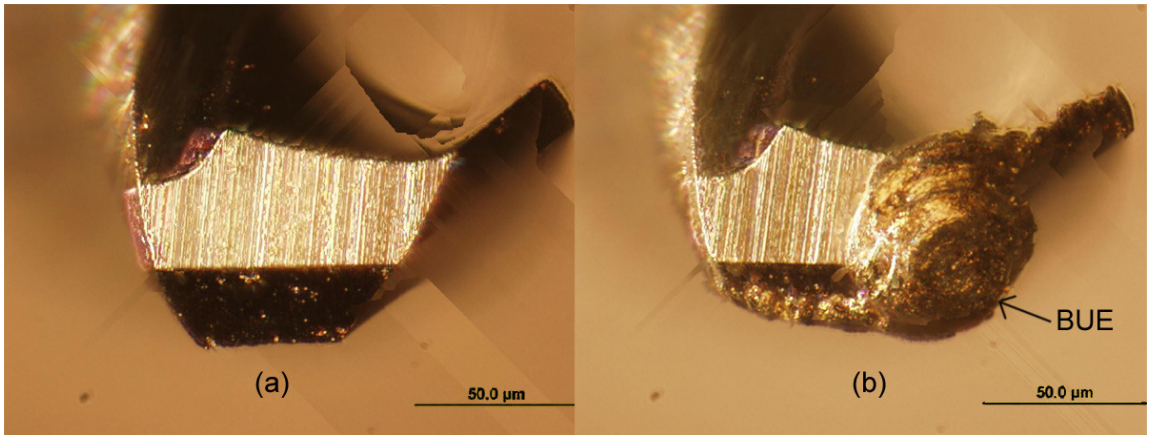

Figure 30: Large built up edge formed on the chisel edge of an uncoated WC Ø127 µm microdrill. (a) New tool and (b) BUE after drilling 20 holes (16.0mm) on Nitinol. Vc=3.2 m/min, 0.02 µm chip load, with CL2210 micromist.

As drilling progressed, this built up edge tended to break off from the tool, in turn taking small sections of the tool along with it. The resulting notch wear is clearly visible in Figure 31. This type of wear was noted to have an adverse effect on drill wandering, as will be discussed in further detail in proceeding sections. Nevertheless, the cutting edge wear rate measured significantly less than the rate at 20 m/min. Also, note the presence of a small about of built up edge that remained after etching.

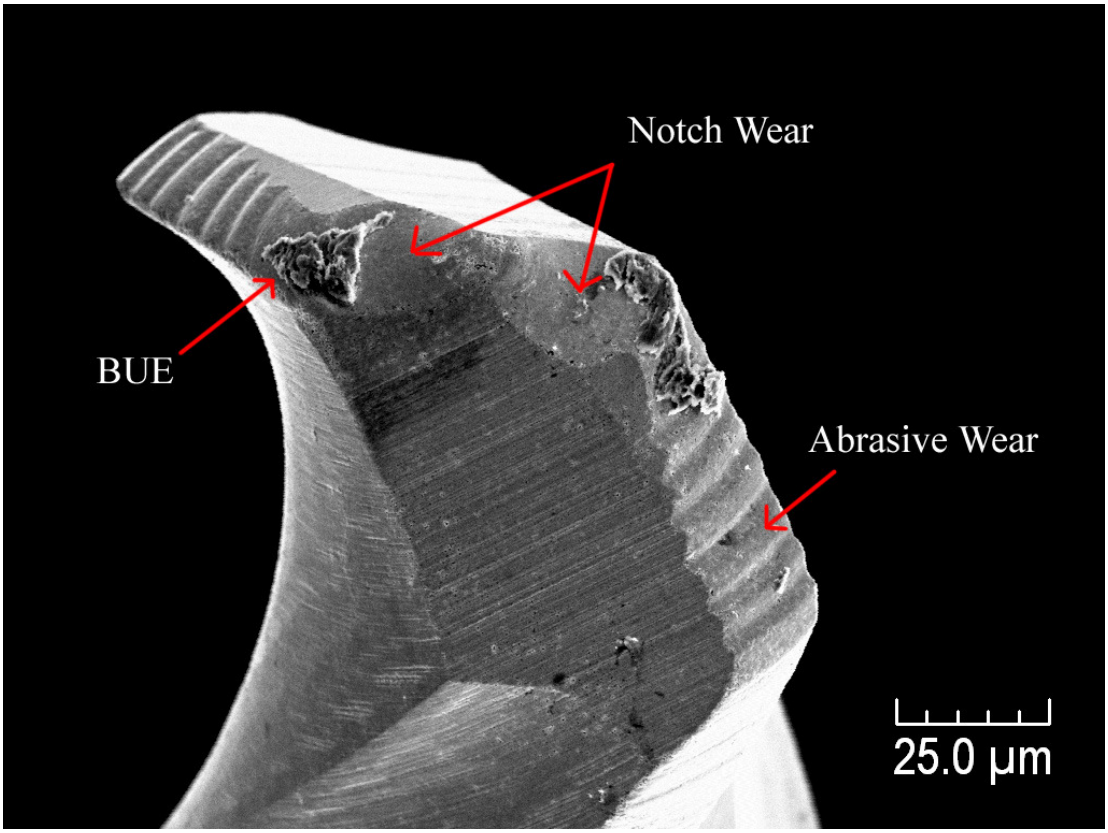

Figure 31: Uncoated WC Ø127 µm microdrill etched after drilling 80 holes (64.0mm) on Nitinol. Vc=3.2 m/min, 0.02 µm chip load, with CL2210 micromist.

Tool wear was also measured between these two extremes at a cutting speed of 14 m/min and 6.0 m/min. While an improvement of the wear rate was noted when drilling at 14 m/min as compared to 20 m/min, a much greater improvement was realized at a speed of 6.0 m/min. In fact, this wear rate was found to be even less than that measured at a cutting speed of 3.2 m/min. This is believed to be a result of measurement uncertainty due to the presence of a BUE.

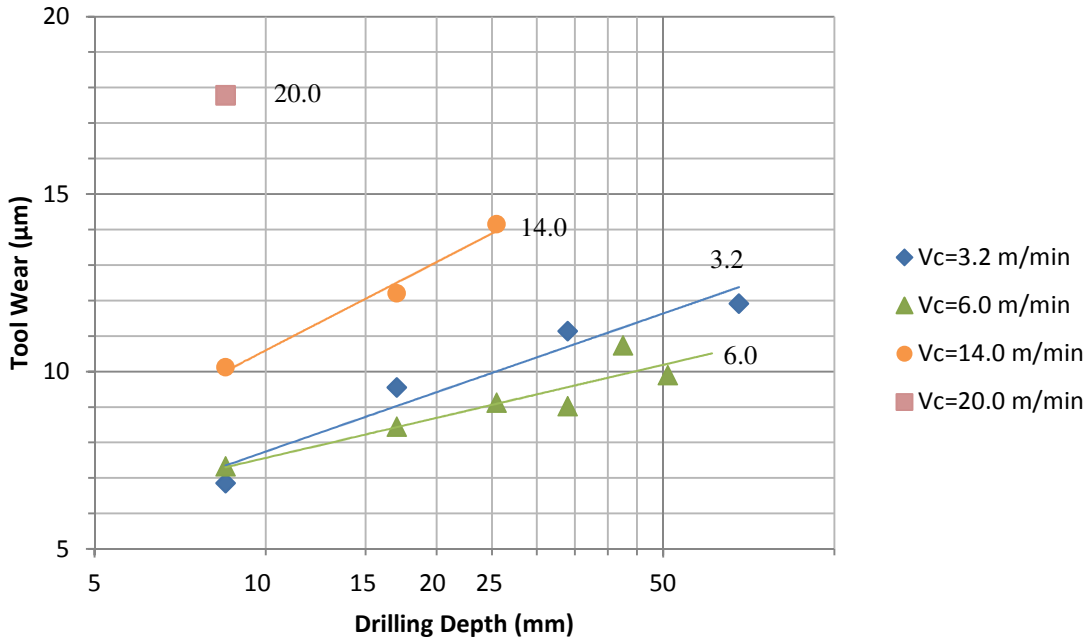

Figure 32: Tool wear vs. drilling depth, uncoated Ø127 µm WC microdrills on Nitinol, 0.02 µm chip load, with CL2210 micromist.

4.3.2 Coated Tools

The wear behavior of the coated tools mimicked that of the uncoated tools with respect to cutting speed (see Figure 33). Again, it was found that the optimum cutting speed was 6.0 m/min for the Nano-tek coated tool. It is uncertain if this was the case for AlTiN coated tools, as they were limited in availability for experimentation. However, in the case of the cutting speed of 14.0 m/min, the AlTiN coated tool outperformed the Nano-tek coated tool.

When compared directly to the uncoated tools, a slight increase in the wear rate of the coated tools for cutting speeds of 3.2 and 6.0 m/min was observed. This may be

attributed to measurement uncertainty; at cutting speeds of 14.0 and 20.0 m/min, this was reversed, and the coated tools showed a drastic improvement in wear resistance.

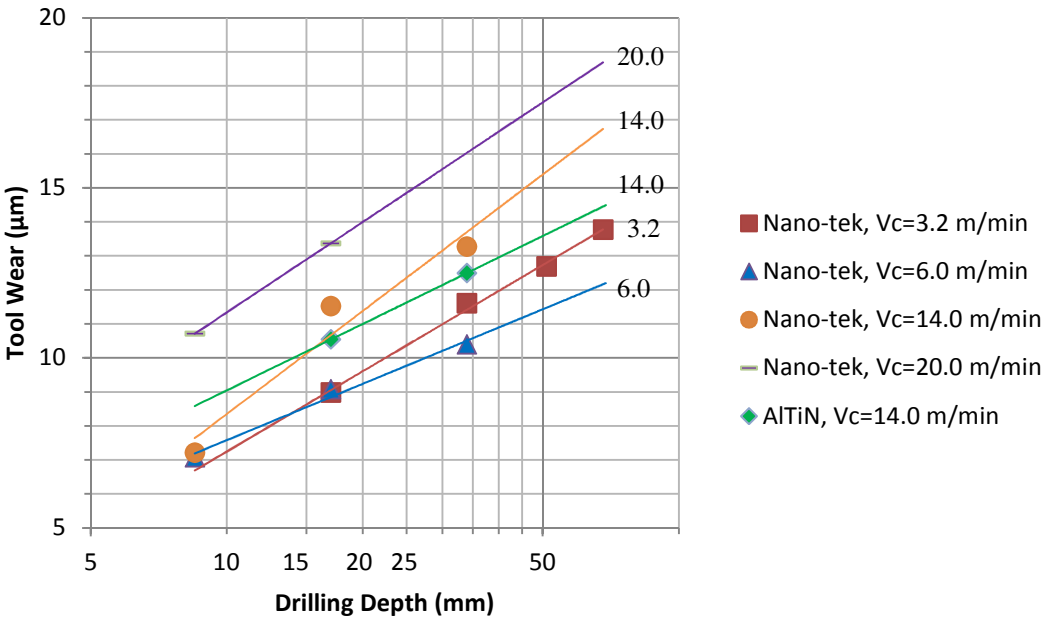

Figure 33: Wear of coated tools vs. drilling depth, Ø127 µm WC microdrills on Nitinol, 0.02 µm chip load with CL2210 micromist.

4.4 Hole Positioning

The primary factors affecting drill positioning accuracy is the spindle runout and wandering of the chisel edge as it enters the workpiece (Lee 1986). Previous research completed on the HAAS OM-2 indicated a runout of less than 1 µm, (Chittipolu 2009) making it an insignificant source of inaccuracy of drill positioning. The positional accuracy of the OM-2 itself was stated as ±5 µm by HAAS, and thus, the large majority of any drill wandering measured could be attributed to the chisel edge. Reduction of the formation of a BUE on the chisel edge proved to be critical in minimizing drill

wandering. Figure 34 shows the average value of centering deviation from its nominal position for all holes drilled until tool failure, with one tool at each cutting speed.

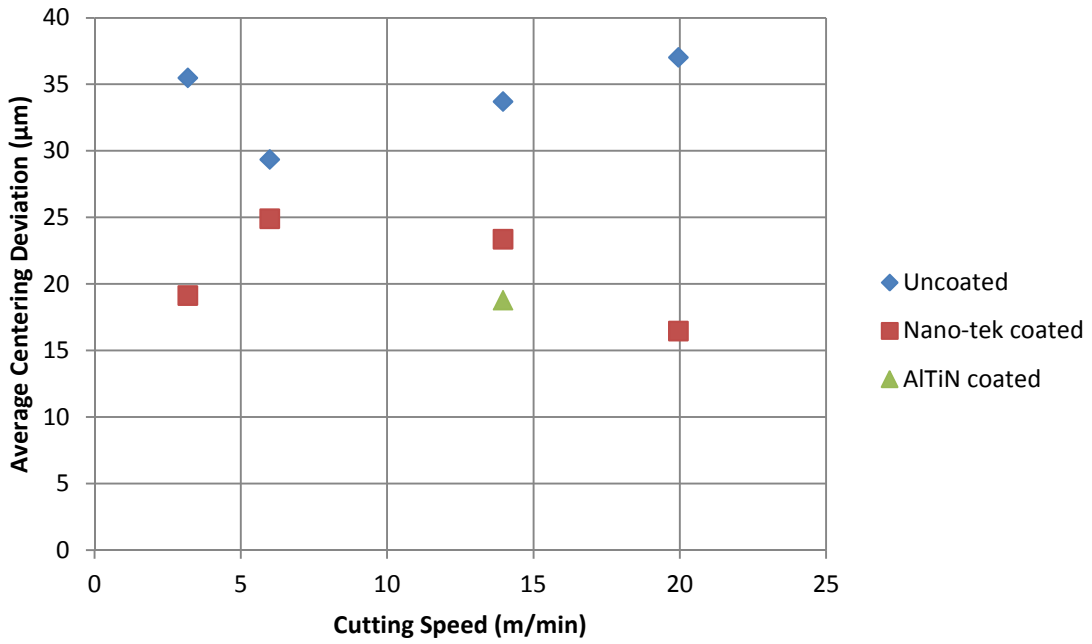

Figure 34: Drill wandering vs. cutting speed for uncoated and coated tools, Ø127 µm WC microdrills, 0.02 µm chip load, with CL2210 micromist

No correlation was noted between the cutting speed and positional accuracy of the holes drilled. However, a substantial improvement was discovered when using coated tools at most cutting speeds (Table 13, Figure 35). This improvement over uncoated is calculated as the percent decrease in average centering deviation between the coated tools and uncoated tools, and can be attributed to the reduction in BUE formation in coated tools. The BUE effectively forms a new, blunt chisel edge that is unable to cut into the Nitinol as easily as a sharp edge, resulting in skidding of the tool as it makes contact with the workpiece surface. The coatings successfully decrease the accumulation

of friction and heat between the tool and workpiece, in turn reducing the size of the BUE.

Table 13: Drill centering deviation

	Average Centering Deviation (µm)			Standard Deviation (µm)			Improvement Over Uncoated (%)	
Vc (m/min)	Uncoated	Nano-tek	AlTiN	Uncoated	Nano-tek	AlTiN	Nano-tek	AlTiN
3.2	35	19	-	19	10	-	46	-
6.0	29	25	-	14	12	-	15	-
14.0	34	23	19	19	12	10	31	44
20.0	37	16	-	18	10	-	56	-

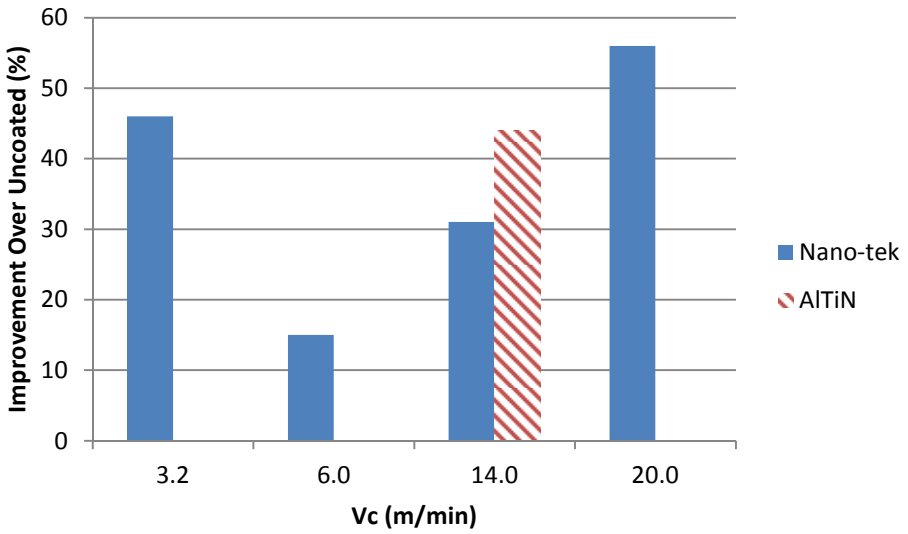

Figure 35: Improved centering accuracy of coated tools versus uncoated tools

Drill wandering as a function of drilling depth was more difficult to quantify due to the random nature of BUE formation - note the increased standard deviation of the

uncoated tools compared to the coated tools in Table 13. A sharp increase in the centering deviation is observed within about the first 10 mm of drilling depth, followed by gradual, nearly linear increase. A similar trend was detected for both uncoated and coated tools, regardless of cutting speed. This is a logical result, because as the chisel edge initially enters the material, it possesses no BUE. The BUE quickly forms on a worn tool's surface/edge after drilling a few holes, resulting in the initial large increase in drill wandering. As the BUE grows, its effect on positional accuracy gradually decreases, but does not cause as large of a change in accuracy as with its initial development. The large variation in centering deviation is explained by the tendency of the BUE to grown and then break off.

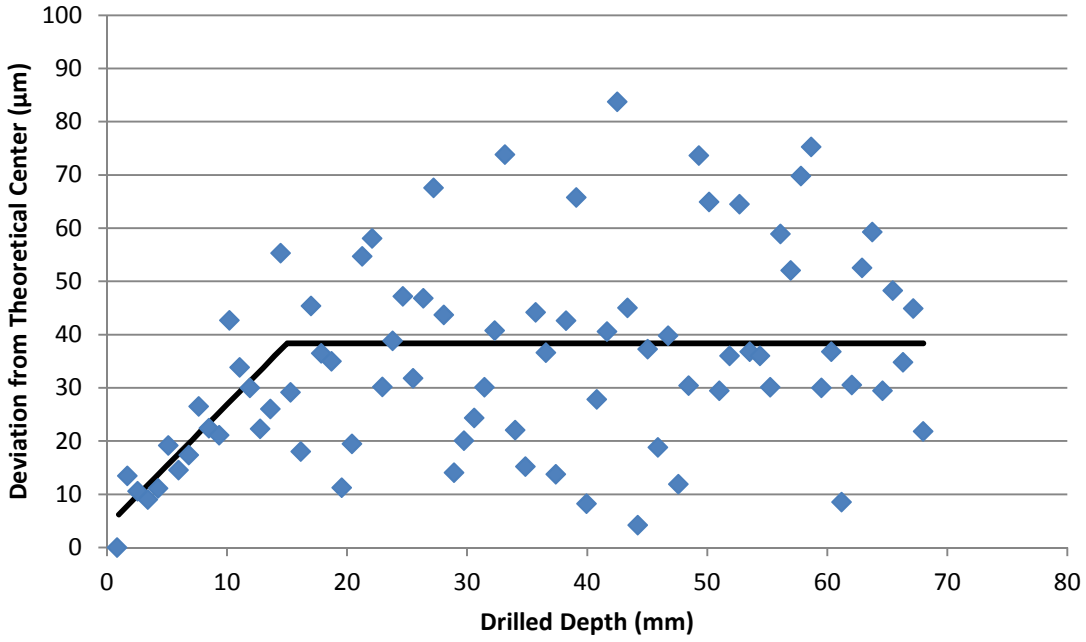

Figure 36: Centering deviation vs. drilling depth, uncoated Ø127 µm WC microdrill on Nitinol, 0.02 µm chip load, Vc=3.2 m/min, with CL2210 micromist.

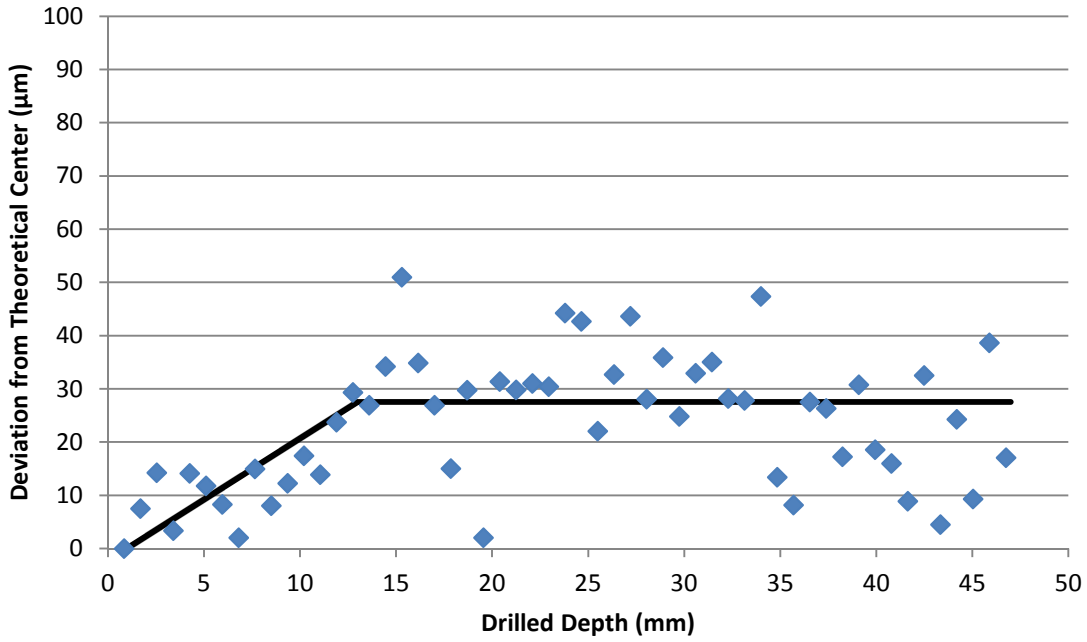

Figure 37: Centering deviation vs. drilling depth, Nano-tek coated Ø127 µm WC microdrill on Nitinol, 0.02 µm chip load, Vc=14.0 m/min, with CL2210 micromist.

When the results are looked at in terms of centering deviation per mm drilled, the trend observed before still holds, with the one exception of the tools cutting at a speed of 6.0 m/min. This, again, may be attributed to measurement uncertainty.

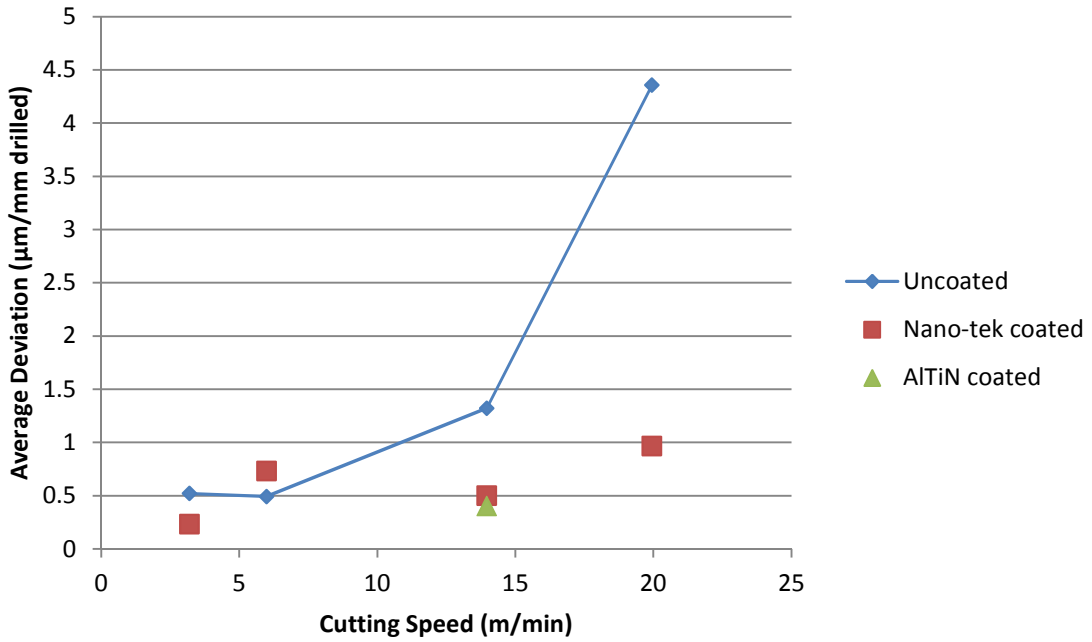

Figure 38: Drill centering deviation per mm drilled at various cutting speeds, uncoated and coated tools, Ø127 µm WC microdrills, 0.02 µm chip load with CL2210 micromist

4.5 Hole Diameter

The general result of the hole diameter variance as a function of drilled depth, and thus, tool wear, can best be described as gradual decline of hole diameter. By taking three measurements of each diameter, very repeatable values were obtained; the average standard deviation of the diameter of each hole was approximately 1 µm. This eliminated any legitimate concern that hole eccentricity may have affected the accuracy of the measurements.

As seen with the analysis of the drill positioning accuracy, the built up edge again plays a role in randomizing the data; the average R^2 value for the linear fit of the hole diameter versus depth drilled was 0.1682 for all tools. However, the overall trend

towards decreasing hole diameter was still readily apparent for almost all tools. As the cutting edges are worn out, the tool's overall diameter is reduced, resulting in smaller holes. Table 14 shows the decrease in diameter as a function of depth drilled, with the first hole being taken as the baseline for measurements, and the diameter of every fifth hole measured.

Table 14: Hole diameter variance for uncoated and coated tools

	Decrease in diameter from starting hole diameter (µm/mm drilled)	
Vc (m/min)	Uncoated	Nano-tek
3.2	0.0456	0.0803
6	0.0169	0.1215
14	-0.0418	0.0802
20	0.017	0.3052

This holds true for uncoated as well as Nano-tek coated tools, although interestingly, the coated tools showed a much more pronounced decrease in diameter. It is believed that this is due to the reduced tendency of the coated tools to form a BUE. When the BUE grows and adheres to the tool, it effectively forms a new cutting edge, resulting in larger diameter holes than would be expected.

4.6 Finite Element Analysis

To analyze tool cutting forces, it is necessary to utilize a model that will be able to accurately describe the process. One such model is the orthogonal cutting model, which simplifies complex, three dimensional machining processes down to only two

dimensions that "play an active role in analysis" (Groover 2010). Assuming the orthogonal model holds for drilling, the drill's cutting edge is straight and perpendicular to cutting velocity.

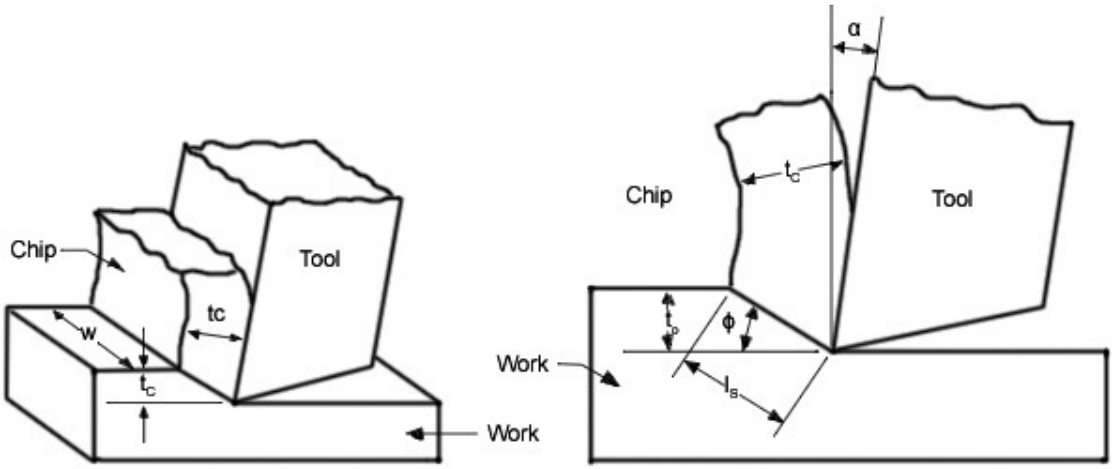

Figure 39: The orthogonal cutting model (Groover, 2010)

Metal cutting is a shearing process, and thus the chip formed by the process can be described by having some thickness t_c being removed from the workpiece along the shear plane, given by the angle ϕ. The rake angle α is the angle that the chip follows after removal from the workpiece. The total shear area, A_S, can be calculated by Equation (8):

$$A_s = \frac{t_o w}{sin\phi} = \frac{F_S}{S_S} \tag{8}$$

Where F_S is the shear force, t_o is the chip load, w is the width of the cutting edge, and S_S is the shear strength of the workpiece material (Groover 2010). Using this relationship and Merchant's Circle, the cutting force F_c and thrust force F_t are given by:

$$F_c = \frac{S_s t_0 w \cos(\beta - \alpha)}{\cos(\phi + \beta - \alpha) \sin \phi} \tag{9}$$

$$F_t = \frac{S_s t_0 w \sin(\beta - \alpha)}{\cos(\phi + \beta - \alpha) \sin \phi} \tag{10}$$

The Merchant equation relates the shear angle, rake angle, and friction angle β by:

$$\phi = 45 + \frac{\alpha}{2} - \frac{\beta}{2} \tag{11}$$

Where β is given by:

$$\beta = \tan^{-1} \mu \tag{12}$$

Thus, with a known coefficient of friction μ and rake angle α, the shear angle can be calculated from Equation (11), and knowing the shear strength of the workpiece material allows for the cutting and thrust forces for a given chip load to be estimated by Equations (9) and (10), respectively.

In addition to the thrust force that arises from the shearing process, an additional axial force can be measured from the plastic deformation due to compression of the workpiece material by the tool. This force can be estimated by:

$$F'_t = S_c A_c \tag{13}$$

In which S_c is the compressive strength of the workpiece material, and A_c is the projected compression area of the tool for a given chip load. This area, shown in Figure 40, increases with increasing chip load until it reaches the outer radius of the tool, from which it will remain constant. The area can easily be calculated by CAD software.

Adding the thrust force F_t and the compressive force F'_t together gives the total axial load experienced by the tool due to the cutting process.

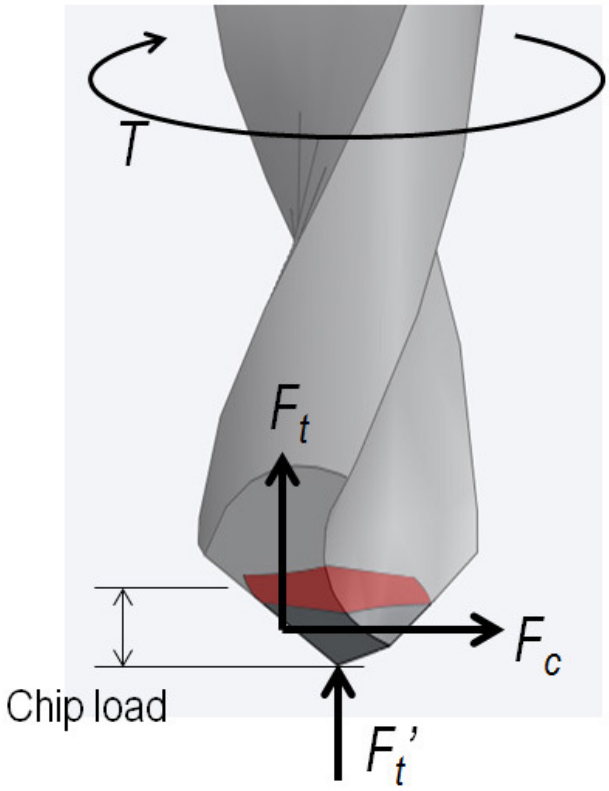

Figure 40: Free body diagram of a micro drill showing projected compression area

Previous research has noted that these axial loads play a role in reducing the effective stress present in the tool when compared to the stress generated solely from the torque caused by the cutting force (Kudla 2011). Experiments on microdrills were completed using pure torsion alone, and pure torsion combined with axial loading. The resulting compression stress from the axial loading causes a stiffening effect that reduces

the overall strain in the tool, and thus decreases the stress. However, care must be taken to ensure that these axial loads do not result in buckling of the tool.

A variety of load cases were then calculated based on the process outlined in section 2.4. To determine the appropriate loads, the coefficient of friction μ between the tungsten carbide tools and Nitinol was needed. A series of experiments (see Appendix C) were run to measure the coefficient of friction using Equation (C.7). This coefficient of friction between the WC tool and Nitinol allowed for the computation of the friction angle β in accordance with Equation (12). With the rake angle α known from Table 4, the shear angle ϕ could then be determined by Equation (11). Next, the shear strength of the Nitinol can be approximated (Oberg et al. 2012) from the known ultimate tensile strength (UTS) from Table 3 by:

$$S_S = 0.6 * UTS = 0.6 * 1625.3MPa = 975.2\ MPa \tag{14}$$

As the tool cutting edge width w was known, the only remaining variable to input into Equations (9) and (10) was the chip load t_o in order to calculate the thrust and cutting forces. An array of chip loads were chosen to test the model until failure occurred.

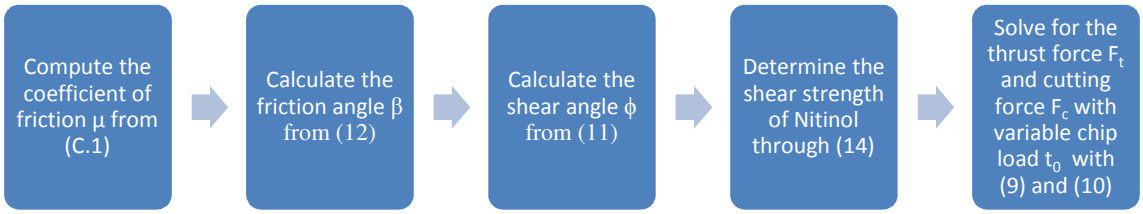

Figure 41: Flow chart outlining the process for calculating the thrust and cutting forces

Two separate analyses were completed using the finite element method: failure due to excessive stress from the combined loading of cutting and thrust forces, and failure due to buckling. Tool failure could be expected at the lowest loading required to reach failure in either of the two loading scenarios. The buckling analysis considered a tool with the chisel and cutting edges fixed, as if already inside a hole, and applied an axial load until failure occurred. This axial load was taken to be the combination of the thrust force generated by cutting (Equation (10)) and the reaction force from the from the workpiece material to the tool (Equation (13)). Thus, the applied axial load was solely a function of the chip load. Upon applying this load to the tool, SolidWorks would calculate a buckling load factor, which is likened to a factor of safety. For factors less than or equal to 1, buckling was predicted; for factors greater than 1 buckling was not predicted.

For example, if a load of 10 N was applied and the buckling factor was calculated to be 1.8, buckling would occur only if a force of 18 N was applied. To

simplify these calculations, a load of 1 N was applied for each tool length, and thus the buckling load factor itself would give the true load required to induce buckling.

The combined loading analysis utilized the thrust and compressive axial loads with the torque generated by the cutting force to determine the equivalent stress in the tool. The torque applied to the tool could easily be calculated by multiplying the cutting force (Equation (9)) by the moment arm, which in this case is taken to be equivalent to the cutting edge length w. These loads were then applied to the tool until the Von Mises stress reached the yield strength of the tungsten carbide tool. Because tungsten carbide is a very brittle material, its yield strength is essentially equivalent to its ultimate tensile strength, which is approximately half its transverse rupture strength (ASTM International 2010).

The purpose of analyzing the tool's behavior using finite element modeling was to use the results to be able to predict failure loads under a variety of cutting conditions, thus enabling the user to identify absolute maximum chip loads and cutting speeds for a given tool. The material properties of the tungsten carbide tool used for analysis are shown in

Table 6. To confirm the validity of the model, the predicted loads as well as stresses calculated from the finite element model using these loads were compared against experimental data obtained, as well as data published in separate studies by Kudla (2011) and Guo (2004).

Kudla utilized static torsion tests to apply a moment around a 0.2mm diameter micro grain carbide twist drill and calculate the maximum shear stress experienced. With this data, a direct comparison of the finite element model can be made, but no correlation can be drawn between the accuracy of the mathematical model. Using SolidWorks' simulation package, the stress intensity was calculated with pure torsion applied to the outer diameter of the tool. This stress intensity is defined as the difference between the largest and the smallest principal stresses. By dividing the stress intensity by 2, the maximum shear stress is calculated (Chen and Han 2007).

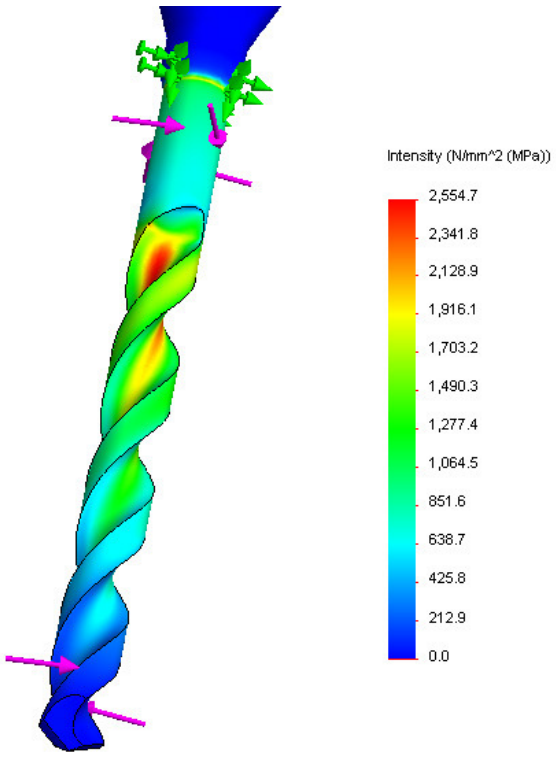

Figure 42: Stress intensity results with a torque of 0.8 N-mm

Using this process, FEA was performed on a 0.2mm diameter drill model, with torque applied at five separate values. The results from this study are compared to the experimental values determined by Kudla in Table 15:

Table 15: FEA results compared to experimental values published by Kudla

Torque (N-mm)	FEM Max Shear (MPa)	Experimental Max Shear (MPa)	Percent Error
0.2	319	270	18.3
0.4	639	540	18.4
0.6	959	810	18.4
0.8	1277	1080	18.3
1.0	1599	1350	18.4

Tool failure occurred in Kudla's experiments at approximately 1.0 N-mm. The results of the FEM study showed an overestimation of the maximum shear stress by a near consistent 18.4 percent for increasing values of torque. Some of this error can be explained by imprecisely modeled geometry and mechanical properties of the carbide, as well as by the presence of small imperfections in the drill.

The data from Guo's experiments allows for a direction comparison of the theoretical loads calculated from the orthogonal cutting model and the true forces that arise from actual drilling. Guo's studies used a 1.0 mm diameter tool with 11L17 steel as the workpiece material. This data is compiled in Table 16.

To illustrate the use of the orthogonal cutting model to calculate theoretical loads, the torque and thrust values shown for a chip load of 101.6 μm (one of the chip loads used by Guo) with a 1.0 mm diameter tool in Table 16 will be derived. First, the compression area of the tool is determined using a 3-D model of the tool as shown in Figure 40. Multiplying this area by the ultimate compressive strength of 11L17 steel of 595 MPa (Harvey 1982) gives the force due to compressive plastic deformation of the steel:

$$F'_t = S_c A_c = 63315.58\mu m^2 * 595 MPa = 37.67N \quad (15)$$

Next, the thrust force that arises from drilling is calculated by using Equation (10):

$$F_t = \frac{S_s t_0 w \sin(\beta - \alpha)}{\cos(\phi + \beta - \alpha)\sin\phi}$$

$$= \frac{0.6 * 595 * 10^6 Pa * 101.6 * 10^{-6} m * 0.5 * 10^{-3} m * \sin(9.202° - 38°)}{\cos(59.4° + 9.202° - 38°) * \sin 59.4°} \quad (16)$$

$$= 11.79N$$

By combining these two forces, the total axial force on the drill is given:

$$F_A = F'_t + F_t = 37.67N + 11.79N = 49.46N \quad (17)$$

Next, the cutting force must be determined with Equation (9):

$$F_c = \frac{S_s t_0 w \cos(\beta - \alpha)}{\cos(\phi + \beta - \alpha)\sin\phi}$$

$$= \frac{0.6 * 595 * 10^6 Pa * 101.6 * 10^{-6} m * 0.5 * 10^{-3} m * \cos(9.202° - 38°)}{\cos(59.4° + 9.202° - 38°) * \sin 59.4°} \quad (18)$$

$$= 21.45N$$

From this, the moment applied on a 1.0mm diameter drill is:

$$M = 21.45N * \frac{1.0 * 10^{-3} m}{2} = 0.0107\ Nm \quad (19)$$

Using the above outlined process, further calculations were performed to compare theoretical values to the experimental data published by Guo:

Table 16: Orthogonal cutting model results compared to experimental values, uncoated WC Ø1.0 mm drill in 11L17 steel (Guo 2004)

Chip Load (µm)	101.6			127			152.4		
S=10,000 rpm	Theoretical	Experimental	Percent Error	Theoretical	Experimental	Percent Error	Theoretical	Experimental	Percent Error
Torque (N-m)	0.0107	0.0145	26.03	0.0134	0.0171	21.60	0.0161	0.0181	11.11
Axial Force (N)	49.46	47.02	5.20	67.27	57.96	16.07	84.43	66.38	27.18

Chip Load (µm)	101.6			127			152.4		
S=20,000 rpm	Theoretical	Experimental	Percent Error	Theoretical	Experimental	Percent Error	Theoretical	Experimental	Percent Error
Torque (N-m)	0.0107	0.0142	24.47	0.0134	0.0148	9.41	0.0161	0.0163	1.30
Axial Force (N)	49.46	45.21	9.41	67.27	53.82	25.00	84.43	62.42	35.25

Chip Load (µm)	101.6			127			152.4		
S=30,000 rpm	Theoretical	Experimental	Percent Error	Theoretical	Experimental	Percent Error	Theoretical	Experimental	Percent Error
Torque (N-m)	0.0107	0.0144	25.52	0.0134	0.0156	14.06	0.0161	0.0167	3.66
Axial Force (N)	49.46	45.68	8.29	67.27	56.2	19.71	84.43	64.41	31.07

One important thing to note is that the orthogonal cutting model does not factor into account the dynamics of a rotating tool, and as such, the theoretical values of the torque and thrust force are constant for all cutting speeds. This is clearly not the case; Guo's data suggests that there is a statistically significant correlation between the chip load and speed and the torque, as well as a correlation between the chip load and thrust force. No correlation was found between the speed and the thrust force. Furthermore, the

orthogonal cutting model assumes a uniform distribution of the cutting forces across the cutting edge, which is not the case for drilling.

With the results of these comparisons in relatively good agreement, both the orthogonal cutting model and finite element model could be used to predict tool failure when drilling various materials. The drill can fail either by buckling due to excessive axial compression loads, by torsion from high cutting forces, or a combination of these. A buckling analysis was completed using SolidWorks models of a 0.15mm diameter uncoated tungsten carbide tool with flute lengths of 1.5mm, 2.5mm, and 3.5mm. The tool was set in a fixed position along the chisel edge to simulate the tool biting into the material.

Table 17: Tools and their respective predicted buckling loads, 2 flute Ø150 µm WC drill on Nitinol

Drill flute length (mm)	Buckling load (N)	Chip load at buckling (µm/flute)
1.5	25.94	325
2.5	10.02	45
3.5	5.52	25

The first material chosen to verify the model was Nitinol. Failure due to torsion was predicted at a chip load of approximately 45µm, and the buckling load was not expected to be an issue except for the 3.5mm long drill. That is, the tool would fail in torsion before it reached the critical buckling load for the 1.5mm and 2.5mm length drill. The 3.5mm long drill was predicted to fail due to buckling with a 5.52 N axial load, equated by the orthogonal cutting model to a chip load of 25µm. Experimental drilling

began with a 1.5mm long drill, and started at a chip load of 0.02μm, as previous success had been achieved drilling at this load. Two holes at each chip load were drilled, and the chip load was then increased by 0.02μm. Cutting speeds of 3.2, 6.0, and 14.0 m/min were used, and the drilling program was modified to accommodate the larger diameter tool (see Appendix A.3).

Table 18: Mechanical properties of test materials

	Nitinol[1]	Al 6061-T6[2]	11L17 steel[3]
Compressive Strength (GPa)	1.625	0.31	0.595
Shear Strength (GPa)	0.9378	0.207	0.343

[1] (Memry Corporation 2011)
[2] (Holt 1996)
[3] (Harvey 1982)

For the 3.2 and 6.0 m/min cutting speeds, the maximum chip load achieved drilling Nitinol was 0.04μm, and 0.02μm was the maximum chip load for speeds of 14.0 m/min. It is hypothesized that this drastic difference between the theoretical and experimental chip load is due to the presence of a large built up edge, as shown in Figure 43. This large formation on the tool causes an extreme increase of forces as it welds the chisel edge and cutting edges of the tool to the workpiece material.

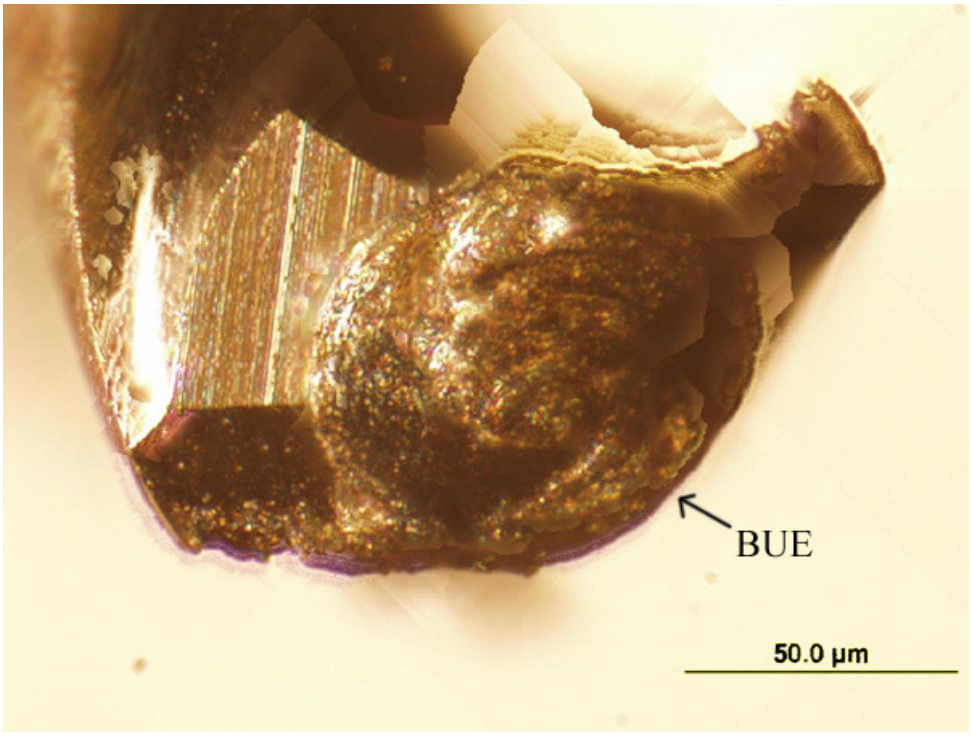

Figure 43: Built up edge of Nitinol on a WC tool after drilling 2 holes for a total depth of 1.7 mm, chip load= 0.02µm, Vc= 3.2 m/min, with CL2210 micromist

The development of such a large BUE after drilling only two holes was surprising. By observing what remained of the fractured tool, it was noticed that it appeared to fail due to torsion developing due to the BUE, with a 45° fracture angle clearly visible. The location of the fracture is in excellent agreement with the location of the maximum shear stress predicted by the finite element model (see Figure 42).

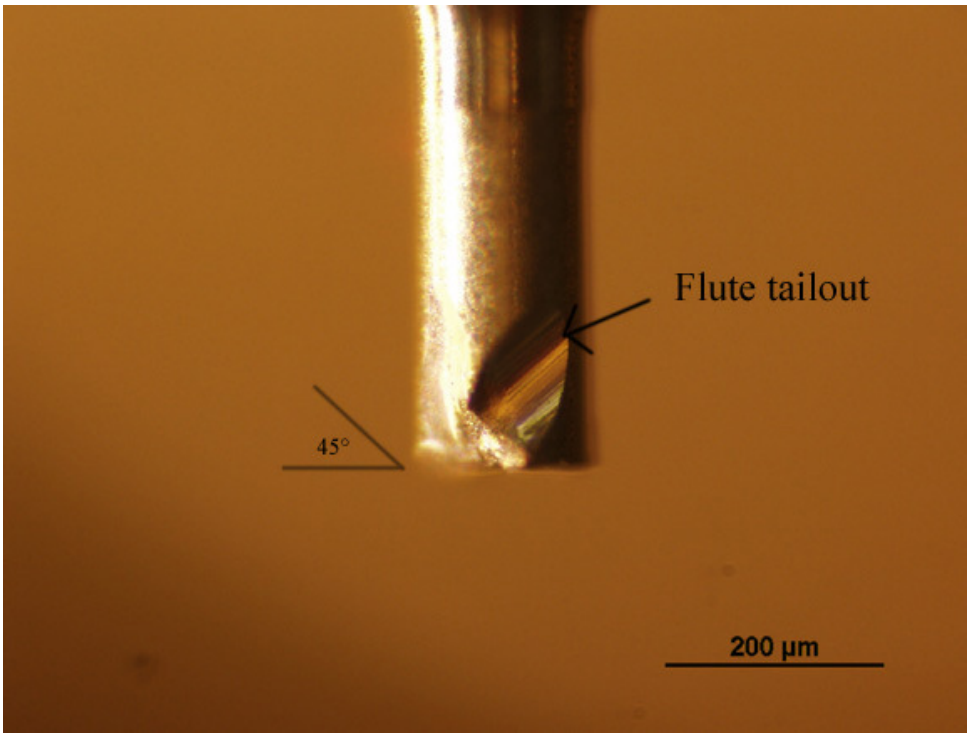

Figure 44: Tool failure due to the large BUE formed drilling Nitinol, viewed at the flute tailout. Ø150 µm uncoated WC microdrill, flute length of 1.5mm, Vc=3.2 m/min, chip load =0.04µm, with CL2210 micromist

Due to the unpredictable nature of the forces involved in the creation of a BUE, a more machinable material was needed to test the model; Aluminum 6061-T6 was selected to fulfill this role. The same process as used for drilling Nitinol was followed. The maximum chip load predicted with the orthogonal cutting model was 210µm/flute, and buckling was not expected to be an issue for any length drill. With a cutting speed of 3.2 m/min, the maximum chip load achieved was only 0.18µm/flute before tool failure. This, again, was most likely due to BUE formation around the chisel edge, as the low cutting speeds created an increase of friction between the tool and workpiece material (Figure 45).

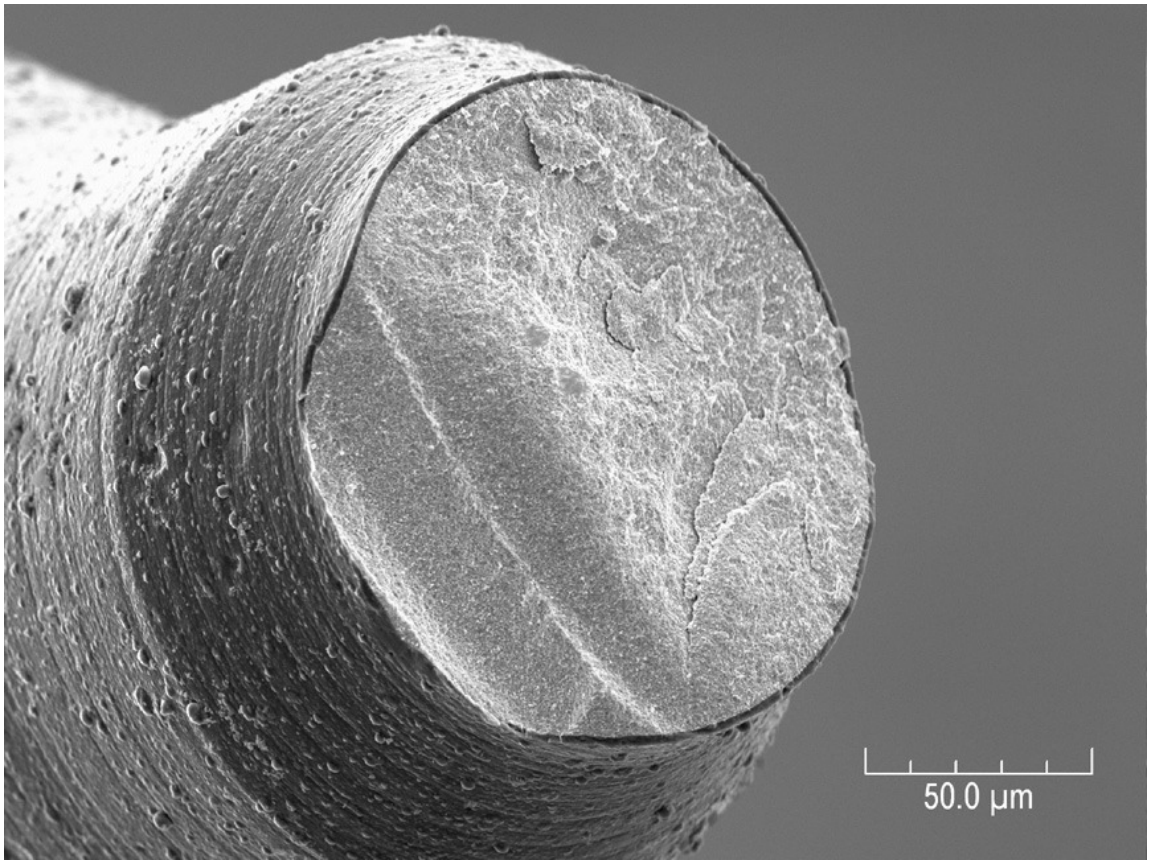

Figure 45: Tool failure due to the large BUE drilling Al 6061-T6, viewed at the top of the flute. Ø150 µm uncoated WC microdrill, flute length of 1.5mm, Vc=3.2 m/min, chip load =0.18µm/flute, with CL2210 micromist

The cutting speed was then increased to 14.0 m/min to reduce the formation of the BUE, and a dramatic improvement was noticed. The feed was increased to the maximum feedrate capability of the OM-2 system (12.7 m/min), which was equivalent to a 175µm/flute chip load, and the tools did not fail for any length drills.

4.7 Burr Formation

While a quantitative analysis of the burrs formed during the drilling process was not within the scope of this research, it is still worthwhile to take a qualitative look at their formation. The surface finish of Nitinol has shown to be of critical importance for the fatigue life of the material (Patel and Gordon 2006), making it essential to minimize burr formation. The general trend appeared to follow that of the tool wear; that is, there was an increase in burr formation as the tool experienced more wear.

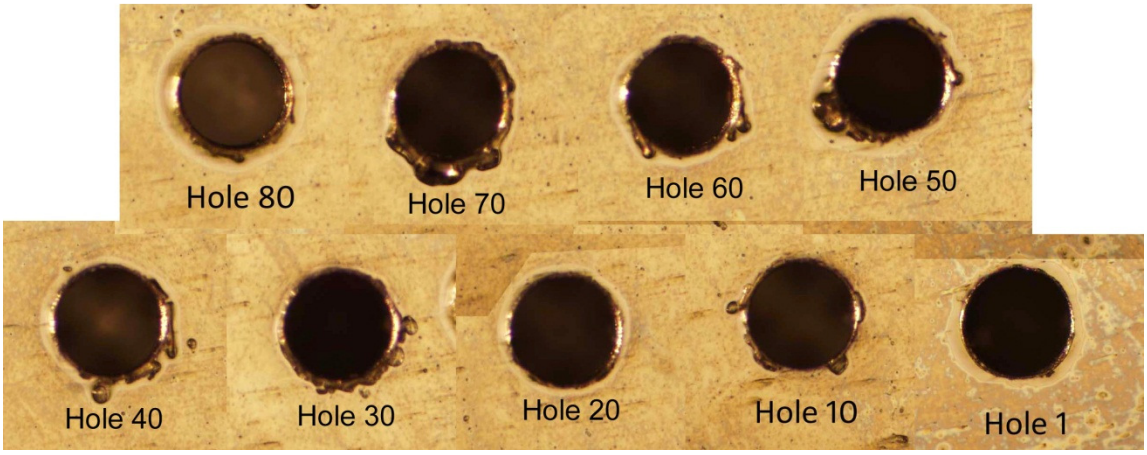

Figure 46: Entry burr formation with an uncoated Ø127 µm WC tool on Nitinol, Vc=3.2 m/min, chip load =0.02µm/flute, with CL2210 micromist

A worn tool is less effective in shearing the workpiece material to form chips, and instead tends to plastically deform the material, pushing it out of the hole to form burrs on the surface. The BUE also effectively blunts the sharp cutting edges of the tool, which results in a similar burr formation mechanism as simple tool wear.

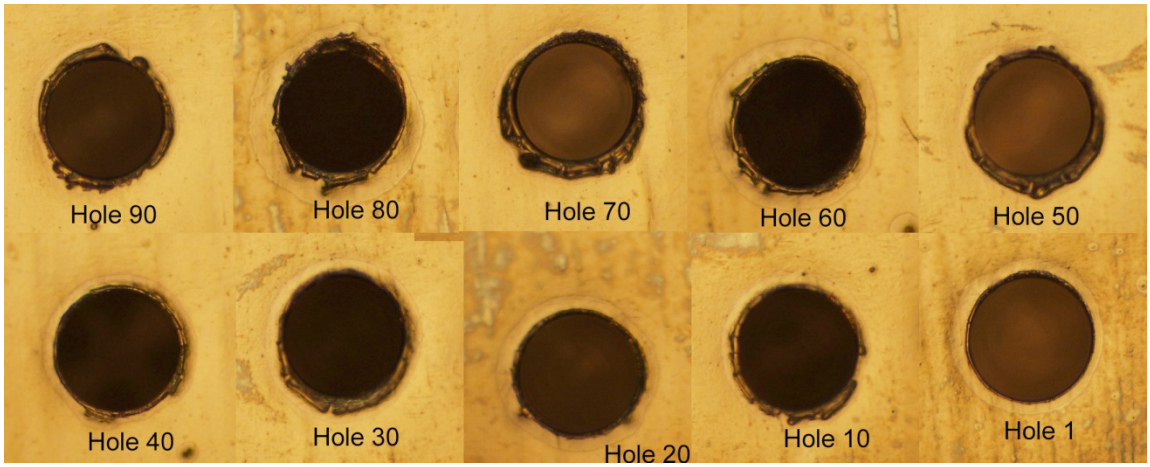

Figure 47: Entry burr formation with a Nano-tek coated Ø127 µm tool on Nitinol, Vc=3.2 m/min, chip load =0.02µm/flute, with CL2210 micromist

Comparing the uncoated tools to the Nano-tek coated tools reveals a slight improvement in hole quality when using the coated tool. While the overall size of the burrs appear to be nearly the same, the burrs formed by the coated tools appear more uniform and with fewer sharp, jagged edges than those formed by the uncoated tools. These sharp edges can result in stress concentrations when a drilled part is subjected to loading, which in turn leads to a decrease in fatigue life (Davidson 2007).

5. CONCLUSIONS

By studying microdrilling of Nitinol and Aluminum, it was found that:

1. Use of Coolube 2210 or similar products is ideal for maximizing the surface wetting of Nitinol and tungsten carbide tools, as well as Nano-tek and AlTiN coatings. This greater surface wetting effectively cools and lubricates the tool, which is critical for successful deep hole microdrilling.
2. Polishing of the surface of Nitinol and peck drilling are essential for quality drilled holes.
3. A larger built up edge is formed with low cutting speeds, leading to notch wear along the chisel edge, but excessively high cutting speeds lead to increased abrasive wear on the cutting edges. The most successful cutting conditions for a ϕ127 μm tool balanced these two wear mechanisms at a cutting speed of 6.0 m/min and chip load of 0.02 μm/tooth for both uncoated and coated tools.
4. Controlling and minimizing the formation of the BUE is necessary for improving hole quality and reducing drill wandering. AlTiN and Nano-tek coated tools proved highly effective in reducing the BUE on the chisel edge, which acted to blunt the chisel edge and increase skidding motion as the drill began to enter the workpiece.
5. Nano-tek and AlTiN coatings were successful in reducing tool wear at higher cutting speeds ($\geq$14.0 m/min), but provided no clear benefit at lower cutting

speeds (≤6.0 m/min) due to the overall reduction of wear in both coated and uncoated tools.

6. Current cutting models and finite element analysis prove ineffective in predicting catastrophic tool failure since the model assumes no BUE formation. The BUE formation on the chisel edge limits the chip load to values far below those predicted by the orthogonal cutting model.

6. RECOMMENDATIONS

Future work on microdrilling of Nitinol should include:

1. An array of different coatings - such as TiCN and CBC with a thickness of ~1.5 μm - should be studied to determine the optimum solution for microdrilling of Nitinol.
2. Cutting speeds in proximity to 6.0 m/min and chip loads near 0.02 μm for Nitinol should be investigated to determine if tool wear can be minimized any further. Furthermore, higher cutting speeds have been shown to reduce BUE, and thus it would be worthwhile to investigate the effects of machining with a greater spindle speed.
3. Finite element modeling that takes into account the dynamics of the tool as well as thermal interaction between the tool and workpiece could prove beneficial in improving its accuracy.
4. Further research into mathematical modeling of built up edge formation to predict maximum chip loads should be conducted.

REFERENCES

Allen, D., H. Almond, and P. Logan. 2000. "A Technical Comparison of Micro-Electrodischarge Machining, Microdrilling, Copper Vapour Laser Machining for the Fabrication of Ink Jet Nozzles." *Proc. SPIE* v4019:531-540.

ASTM International 2010. "ASTM Standard B528-10 Standard Method for Transverse Rupture Strength of Metal Powder Specimens." West Conshohocken, PA.

Azar, J.J. and G. R. Samuel. 2007. *Drilling Engineering*. Tulsa, OK: PennWell Corp.

Beer, Ferdinand P., E. R. Johnston, Elliot R. Eisenberg, and George H. Staab. 2003. *Vector Mechanics for Engineers - Statics*. 7th ed. Boston: McGraw-Hill.

Biermann, D., F. Kahleyss, E. Krebs, and T. Upmeier. 2010. "A Study on Micro-Machining Technology for the Machining of NiTi: Five-Axis Micro-Milling and Micro Deep-Hole Drilling." *Journal of Materials Engineering and Performance* v20:745-751.

Byrne, G., D. Dornfeld, and B. Denkena. 2003. "Advancing Cutting Technology." *CIRP Annals* v52(2):483-507.

Chen, Wai-Fah and Da-Jian Han. 2007. *Plasticity for Structural Engineers*. New York: J. Ross Publishing.

Chen, J.Z. and S.K. Wu. 1999. "Chemical Machined Thin Foils of TiNi Shape Memory Alloy." *Materials Chemistry and Physics* v58:162-165.

Chittipolu, Sujeev. 2009. "Failure Prediction and Stress Analysis of Micro-Cutting Tools." Masters Thesis, Texas A&M University.

Covidien. 2012. “Protege® GPS™ Self-Expanding Nitinol Biliary Stent System.” Retrieved February 3, 2012 (http://www.ev3.net/peripheral/us/se-biliary-stents/protg-gps-selfexpanding-biliary-stent-system.htm).

Dassault Systemes. 2012. “SolidWorks Help - Tetrahedral Elements.” Retrieved October 12, 2012 (http://help.solidworks.com/2013/English/SolidWorks/cosmosxpresshelp/c_Tetrahedral_Elements.htm).

Davidson, David A. 2007. “Surface Condition Impacts Part Performance: Burrs, Edges can Negatively Influence Function of Components.” *Metal Finishing* v105(2):22-31.

Dormfeld, D., S. Min, and Y. Takeuchi. 2006. “Recent Advances in Mechanical Micromachining.” *Annals of the CIRP* v55(2):745-768.

Gong, Yongping, Kornel F. Ehmann, and Cheng Lin. 2003. “Analysis of Dynamic Characteristics of Micro-Drills.” *Journal of Materials Processing Technology* v141:16-28.

Gould, John V. 1963. “Machinability of Nickel - Titanium Alloys.” Metcut Research Associates, Inc., Cincinnati.

Groover, Mikell P. 2010. *Fundamentals of Modern Manufacturing: Materials, Processes, and Systems, 4th Edition*. Hoboken, NJ: J. Wiley & Sons.

Guo, Anping. 2004. “Investigation of the Static and Dynamic Characteristics of Micro-Drilling.” PhD Dissertation, University of Arkansas.

HAAS Automation, Inc. 2012. Retrieved January 23, 2012 (http://www.haascnc.com).

Harvey, Philip D. 1982. *Engineering Properties of Steels*. Materials Park, OH: American Society for Metals.

Henkel Corporation. 2010. "Technical Data Sheet - Loctite Super Glue." Retrieved October 7, 2012 (http://www.loctiteproducts.com/tds/SG_BOTTLE_tds.pdf).

Holt, John M. 1996. *Structural Alloys Handbook*. West Lafayette, Ind.: Purdue University Center for Information and Numerical Data Analysis and Synthesis.

Huang, Han. 2004. "A Study of High-Speed Milling Characteristics of Nitinol." *Materials and Manufacturing Processes* v19:159-175.

Hung, N.P. 2012. *Machinery's Handbook 29th Edition*. New York: Industrial Press.

Imran, M., P.T. Mativenga, S Kannan, and D. Novovic. 2008. "An Experimental Iinvestigation of Deep-Hole Microdrilling Capability for a Nickel-Based Superalloy." *Proc. IMechE* v222(B):1589-1596.

Kauffman, George and Isaac Mayo. 1996. "The Story of Nitinol: The Serendipitous Discovery of the Memory Metal and Its Applications." *The Chemical Educator* v2(2):1-21.

Kudla, Leszek A. 2011. "Fracture Phenomena of Microdrills in Static and Dynamic Conditions." *Engineering Fracture Mechanics* v78(1):1-12.

Lee, S.J. 1986. "The Influence of Drill Characteristics and Entry Mechanisms on Drilling Performance." PhD Thesis, University of Wisconsin-Madison.

Lendlein, A. and S. Kelch. 2002. "Shape-Memory Polymers." *Angewandte Chemie Int. Ed. 41* 2034-2057.

Martin, Don and Robin Wilcox. 1990. “Spindle Runout Effects on Positional Accuracy.” Symposium on Small Hole Technology Conference Proceedings, Palm Springs, CA.

McCabe, M.J. 2001. “How PVD Coatings Can Improve High Speed Machining.” High Speed Machining Conference Proceedings, Northbrook, IL.

Memry Corporation. 2011. “Certificate of Conformity.” Bethel, Connecticut.

Mitsubishi Materials Corporation. 2007. “GRADE INFORMATION (ROTARY BLANKS).” Retrieved June 11, 2011 (http://blank.mitsubishicarbide.com/mmc/en/product/material/index.html).

Mohanty, Sankalp. 2011. “Microdrilling of Biocompatible Materials.” Masters Thesis, Texas A&M University.

Nanomechanics. 2013. “Nano- Versus Micro- Indentation Hardness.” Retrieved February 17, 2013 (http://nanomechanicsinc.com/service-lab/vickers-hardness-conversion).

Oberg, Erik, Holbrook Horton, Franklin Jones, and Henry Ryffel. 2012. *Machinery's Handbook 29th Edition*. New York: Industrial Press.

Patel, Mitesh M. and Richard F. Gordon. 2006. “An Investigation of Diverse Surface Finishes on Fatigue Properties of Superelastic Nitinol Wire.” Presentation at The International Conference on Shape Memory and Superelastic Technologies, Fort Wayne.

Pelton, A.R., D. Stockel, and T.W. Duerig. 2000. “Medical Uses of Nitinol.” *Materials Science Forum* v327-328:63-70.

Performance Micro Tool. 2012. “Performance Micro Tool - Solid Carbide Micro Tools.” Retrieved March 18, 2012 (http://www.pmtnow.com/index.htm).

PVD Coatings. 2013. “Coating Thickness Tester.” Retrieved February 23, 2013 (http://www.pvd-coatings.co.uk/pvd-coating-technology/testing-equipment/coating-thickness-tester/).

Rahman, M., A. Senthil Kumar, and M.U. Salam. 2002. “Experimental Evaluation on the Effect of Minimal Quantities of Lubricant in Milling.” *International Journal of Machine Tools and Manufacture* v42(5):539-547.

Shabalovskaya, S.A. 2002. “Surface, Corrosion and Biocompatibility Aspects of Nitinol as an Implant Material.” *Bio-Medical Materials and Engineering* v12:69-109.

Socorex Isba S.A. 2012. “Micropipettes - Acura Manual 825 - Adjustable Volume Micropipettes.” Retrieved October 7, 2012 (http://www.socorex.com/digital-reading-micropipettes-acura-manual-en-1-0-5-5.html).

Sproul, William D. 1996. “Physical Vapor Deposition Tool Coatings.” *Surface and Coatings Technology* v81:1-7.

Stephenson, David and John Agapiou. 2006. *Metal Cutting Theory and Practice*. Boca Raton, FL: CRC Taylor & Francis.

Subramanian, C. and K.N. Strafford. 1993. “Review of Multicomponent and Multilayer Coatings for Tribological Applications.” *Wear* v165:85-95.

Swiss-Tek Coating Inc. 2010. “Swiss-Tek Coating Inc. - Coating Properties - PVD Coating Datasheet.” Retrieved December 15, 2011 (http://www.swiss-tekcoatings.com/properties.html).

Tansel, I., O. Rodriguez, M. Trujillo, E. Paz, and W. Li. 1998. “Micro-End-Milling - I. Wear and Breakage.” *International Journal of Machine Tools & Manufacture* v38(12):1419-1436.

Thamizhmanii, S., Rosli, and S. Hasan. 2009. “A Study of Minimum Quantity Lubrication on Inconel 718 Steel.” *Archives of Materials Science and Engineering* v39(1):38-44.

Ueng, H.y., C.T. Guo, and K.H. Dittrich. 2006. “Development of a Hybrid Coating Process for Deposition of Diamond-like Carbon Films on Microdrills.” *Surface and Coatings Technology* v200(9):2900-2908.

Weinert, K. and V. Petzoldt. 2006. “Machining NiTi Micro-parts by Micro-milling.” *Materials Science and Engineering* v481-482:672-675.

Weinert, K., V. Petzoldt, D. Kötter, and M. Buschka. 2004. “Drilling of NiTi Shape Memory Alloys.” *Materialwissenschaft und Werkstofftechnik* v35(5):338-341.

APPENDIX A. CNC CODE FOR MICRODRILLING

A.1 Spindle Warm Up Program

```
%
O02026 (NSK 20 MIN SPINDLE WARM-UP)
M03 S10000
G04 P120.
M03 S20000
G04 P180.
M03 S25000
G04 P180.
M03 S30000
G04 P180.
M03 S35000
G04 P180.
M03 S40000
G04 P180.
M03 S50000
G04 P180.
M05
M30
%
```

A.2 Microdrilling Program

```
%
O00016
( Stephen - Drilling Program )
(created 07/31/11)
(For use with 127 micron tool)

N35 G00 G17 G21 G40 G90
(STANDARD START-UP SETTINGS)

N45 T1
(IDENTIFIES TOOLING)
```

```
N50 G55 G00 X0. Y0. Z1.
(MOVES MACHINE TO STARTING COORDINATES)
(COORDINATES SET IN LINE G55 IN OFFSETS)
(MUST SET ZEROES ON UPPER LEFT CORNER OF PART)

N55 G43 H01
(CALLS OUT TOOL LENGTH COMPENSATION)

N60 S35000 M03
(SETS SPINDLE SPEED AND TURNS ON CLOCK-WISE)


N70 M97 P55555 L10
(M97 CALLS FOR SUB-ROUTINE)
(P55555 --> SUBROUTINE AT LINE N55555)
(L10 --> NUMBER OF TIMES TO REPEAT SUBROUTINE)

N75 G90 G55 X0. Y0. Z5.
(RETURNS TOOL TO START POSITION)

N80 M30
(ENDS PROGRAM)
%

%
N55555 G90
G01 Z0.15 F50.
G01 Z-0.254 F1.4 (First peck)
G01 Z1.0 F100. (Retract)
G04 P1.5 (Pauses to cool and flush chips)
G01 Z-0.104 F50. (Position for next peck)
G01 Z-0.487 F1.4 (Second peck)
G01 Z1.0 F100.
G04 P1.5
G01 Z-0.337 F50.
G01 Z-0.649 F1.4 (Third peck)
G01 Z1.0 F100.
```

```
G04 P1.5
G01 Z-0.499 F50.
G01 Z-0.784 F1.4 (Fourth peck)
G01 Z1.0 F100.
G04 P1.5
G01 Z-0.634 F50.
G01 Z-0.90 F1.05 (Fifth peck)
G01 Z1.0 F100.
G04 P1.5

G91 X0.254 F200.
(MOVES INCREMENTAL DISTANCE IN X DIRECTION)
(NOT DEPENDENT UPON COORDINATES)


M99
(RETURNS TO MAIN PROGRAM)
%
```

A.3 Microdrilling Program for Finite Element Verification

```
%
O00017
( Stephen - Drilling Program )
(created 09/15/11)
(For use with 150 micron tool)

N35 G00 G17 G21 G40 G90
(STANDARD START-UP SETTINGS)

N45 T1
(IDENTIFIES TOOLING)

N50 G55 G00 X0. Y0. Z1.
(MOVES MACHINE TO STARTING COORDINATES)
(COORDINATES SET IN LINE G55 IN OFFSETS)
(MUST SET ZEROES ON UPPER LEFT CORNER OF PART)
```

```
N55 G43 H01
(CALLS OUT TOOL LENGTH COMPENSATION)

N60 S35000 M03
(SETS SPINDLE SPEED AND TURNS ON CLOCK-WISE)


N70 M97 P55555 L2
(M97 CALLS FOR SUB-ROUTINE)
(P55555 --> SUBROUTINE AT LINE N55555)
(L2 --> NUMBER OF TIMES TO REPEAT SUBROUTINE)

N80 M30
(ENDS PROGRAM)
%

%
N55555 G90
G01 Z0.15 F50.
G01 Z-0.3 F1.4 (First peck)
G01 Z1.0 F100. (Retract)
G04 P1.5 (Pauses to cool and flush chips)
G01 Z-0.15 F50. (Position for next peck)
G01 Z-0.575 F1.4 (Second peck)
G01 Z1.0 F100.
G04 P1.5
G01 Z-0.425 F50.
G01 Z-0.804 F1.4 (Third peck)
G01 Z1.0 F100.
G04 P1.5
G01 Z-0.654 F50.
G01 Z-0.9 F1.4 (Fourth peck)
G01 Z1.0 F100.
G04 P1.5

G91 X0.3 F200.
(MOVES INCREMENTAL DISTANCE IN X DIRECTION)
(NOT DEPENDENT UPON COORDINATES)
```

```
M99
(RETURNS TO MAIN PROGRAM)
%
```

APPENDIX B. MICRODRILLING DATA

B.1 Tool Wear Data

Table B.1 Tool Wear at Vc=3.2 m/min

S (rpm)	Vc (m/min)							
8000	3.192							
Holes	10	20	30	40	50	60	70	80
Depth (mm)	8.5	17	25.5	34	42.5	51	59.5	68
Uncoated Wear (µm)	6.855	9.55	---	11.14	---	---	---	11.91
Nano-tek Wear (µm)	---	8.98	---	11.605	---	12.685	---	13.77

Table B.2 Tool Wear at Vc=6.0 m/min

S (rpm)	Vc (m/min)							
15000	5.985							
Holes	10	20	30	40	50	60	70	80
Depth (mm)	8.5	17	25.5	34	42.5	51	59.5	68
Uncoated Wear (µm)	7.32	8.445	9.12	9.02	10.73	9.89	---	---
Nano-tek Wear (µm)	7.075	9.08	---	10.39	---	---	---	---

Table B.3 Tool Wear at Vc=14.0 m/min

S (rpm)	Vc (m/min)							
35000	13.964							
Holes	10	20	30	40	50	60	70	80
Depth (mm)	8.5	17	25.5	34	42.5	51	59.5	68
Uncoated Wear (µm)	10.12	12.2	14.15	---	---	---	---	---
Nano-tek Wear (µm)	7.21	11.52	---	13.275	---	---	---	---
AlTiN Wear (µm)	---	10.54	---	12.495	---	---	---	---

Table B.4 Tool Wear at Vc=20.0 m/min

S (rpm)	Vc (m/min)							

50000	19.949							
Holes	10	20	30	40	50	60	70	80
Depth (mm)	8.5	17	25.5	34	42.5	51	59.5	68
Uncoated Wear (µm)	17.785	---	---	---	---	---	---	---
Nano-tek Wear (µm)	10.71	13.37	---	---	---	---	---	---

B.2 Drill Positioning Data

Table B.5 Drill Centering Deviation at Vc=3.2 m/min

Hole	Uncoated Deviation (µm)	Nano-tek Deviation (µm)
1	0	0.00
2	13.45	15.55
3	10.54	3.84
4	9.01	0.96
5	11.08	10.79
6	19.17	9.29
7	14.55	7.39
8	17.37	7.94
9	26.49	6.74
10	22.42	4.50
11	21.10	18.30
12	42.64	11.06
13	33.82	22.62
14	29.98	16.15
15	22.26	19.81
16	26.01	38.40
17	55.28	20.86
18	29.11	16.99
19	18.03	31.94
20	45.37	38.83
21	36.47	22.28
22	34.99	22.01
23	11.23	20.47
24	19.43	13.21
25	54.66	8.62
26	58.04	4.87
27	30.16	5.23
28	38.84	31.77
29	47.14	15.35
30	31.76	10.98
31	46.83	16.00
32	67.55	31.71
33	43.70	10.47
34	14.05	26.90
35	20.06	34.02
36	24.32	8.50
37	30.07	25.08
38	40.72	13.68
39	73.82	15.89
40	22.04	21.87
41	15.20	25.64
42	44.17	9.50
43	36.59	14.19
44	13.76	18.15
45	42.60	18.72
46	65.73	16.21
47	8.21	24.51
48	27.82	18.31
49	40.54	23.99
50	83.69	7.55
51	44.99	10.08
52	4.18	31.89

53	37.27	19.73
54	18.81	30.70
55	39.76	24.08
56	11.91	17.16
57	30.41	12.63
58	73.61	22.48
59	64.87	36.36
60	29.46	42.64
61	35.96	34.35
62	64.51	10.73
63	36.78	30.16
64	35.97	11.18
65	30.12	31.69
66	58.89	27.70
67	52.04	26.02
68	69.77	20.73
69	75.24	8.47
70	29.97	2.90
71	36.78	20.56
72	8.49	8.99
73	30.51	36.15
74	52.50	11.28
75	59.25	12.58
76	29.41	34.70

77	48.24	30.26
78	34.79	29.60
79	44.87	32.87
80	21.82	14.01
81	-	17.18
82	-	6.26
83	-	9.79
84	-	3.16
85	-	29.50
86	-	21.04
87	-	19.23
88	-	13.21
89	-	26.67
90	-	15.32
91	-	9.55
92	-	18.00
93	-	26.31
94	-	30.69
95	-	25.91
96	-	25.95

Table B.6 Drill Centering Deviation at Vc=6.0 m/min

Hole	Uncoated Deviation (µm)	Nano-tek Deviation (µm)
1	0	0.00
2	23.18	17.60
3	15.65	13.75
4	24.44	25.62
5	33.27	18.69
6	13.38	21.56
7	30.92	24.38
8	34.23	24.48
9	20.39	16.34
10	47.41	9.87
11	21.58	15.34
12	22.94	1.84
13	18.57	15.80
14	18.48	17.90
15	15.41	32.50
16	34.39	20.35
17	52.24	11.01
18	36.74	12.50
19	10.26	25.07
20	57.14	19.76
21	7.43	5.32
22	32.60	21.03
23	20.70	28.65
24	12.54	27.64
25	18.98	33.86
26	41.98	15.62
27	25.61	14.54
28	24.12	17.40
29	11.34	32.29
30	41.58	31.94
31	38.19	23.08
32	37.19	50.31
33	24.23	35.51
34	9.57	26.70
35	17.15	39.53
36	46.13	41.18
37	50.13	53.62
38	30.54	39.99
39	14.69	40.99
40	26.19	47.19
41	22.89	-
42	4.53	-
43	12.19	-
44	37.17	-
45	29.24	-
46	50.08	-
47	12.60	-
48	27.56	-
49	65.50	-
50	18.85	-
51	65.19	-
52	31.39	-
53	27.35	-
54	39.66	-
55	33.36	-
56	16.56	-
57	18.57	-
58	60.34	-
59	50.88	-
60	29.52	-
61	19.71	-
62	21.73	-
63	17.14	-
64	35.68	-
65	39.06	-
66	32.85	-
67	24.70	-
68	48.20	-
69	39.46	-
70	30.99	-

Table B.7 Drill Centering Deviation at Vc=14.0 m/min

Hole	Uncoated Deviation (µm)	Nano-tek Deviation (µm)	AlTiN Deviation (µm)
1	0	0.00	0.00
2	4.25	7.49	5.11
3	20.66	14.23	12.63
4	11.39	3.37	1.41
5	18.48	14.08	8.89
6	11.60	11.75	7.73
7	21.16	8.29	0.65
8	17.26	2.00	10.03
9	10.85	14.97	22.12
10	26.13	8.06	4.03
11	46.33	12.23	13.83
12	49.84	17.42	17.53
13	36.53	13.85	4.02
14	10.29	23.70	21.11
15	21.01	29.32	14.16
16	29.90	26.92	27.59
17	17.17	34.16	18.34
18	55.24	50.93	45.16
19	26.66	34.87	29.80
20	68.39	26.89	6.33
21	43.43	15.00	17.90
22	30.44	29.76	27.13
23	52.01	2.04	8.00
24	36.11	31.37	30.68
25	68.53	29.78	29.79
26	41.16	30.98	26.14
27	30.32	30.40	24.80
28	37.92	44.22	36.00
29	67.95	42.65	33.28
30	66.61	22.07	19.83
31	-	32.71	28.33
32	-	43.63	32.41
33	-	28.04	12.07
34	-	35.87	30.35
35	-	24.82	35.07
36	-	32.94	13.33
37	-	35.04	17.24
38	-	28.17	17.94
39	-	27.82	11.46
40	-	47.37	34.26
41	-	13.39	16.76
42	-	8.17	5.09
43	-	27.52	22.83
44	-	26.32	19.38
45	-	17.21	15.77
46	-	30.79	28.34
47	-	18.53	11.93
48	-	15.98	16.41
49	-	8.86	4.46
50	-	32.48	30.54
51	-	4.48	14.63
52	-	24.26	15.11
53	-	9.29	14.86
54	-	38.64	31.42
55	-	17.05	9.77

Table B.8 Drill Centering Deviation at Vc=20.0 m/min

Hole	Uncoated Deviation (µm)	Nano-tek Deviation (µm)
1	0	0.00
2	23.09	37.24
3	33.83	36.74
4	25.53	18.36
5	19.12	28.87
6	40.64	17.31
7	21.09	23.95
8	54.74	8.03
9	71.32	11.41
10	43.83	15.43
11	-	20.89
12	-	23.84
13	-	15.66
14	-	9.94
15	-	10.10
16	-	6.38
17	-	11.45
18	-	4.57
19	-	4.06
20	-	8.53

B.3 Hole Diameter Data

Table B.9 Hole Diameter, Uncoated Tool at Vc=3.2 m/min

Hole Diameter (μm)					
Hole	Measurement 1	Measurement 2	Measurement 3	Average	Std Dev
1	143.25	143.41	142.44	143.03	0.42
5	141.74	141.30	139.93	140.99	0.77
10	141.46	141.64	141.85	141.65	0.16
15	140.84	142.02	141.44	141.44	0.48
20	142.05	142.93	143.38	142.79	0.55
25	147.19	148.89	148.36	148.15	0.71
30	142.42	141.73	144.90	143.02	1.36
35	143.31	143.31	142.15	142.92	0.55
40	136.04	138.44	139.10	137.86	1.32
45	136.91	137.20	137.15	137.09	0.13
50	139.76	140.33	140.96	140.35	0.49
55	142.54	143.96	143.31	143.27	0.58
60	139.17	139.46	140.67	139.77	0.65
65	141.53	141.60	140.62	141.25	0.45
70	138.68	139.92	140.64	139.74	0.81
75	140.39	141.37	141.49	141.09	0.50
80	139.57	139.78	138.81	139.38	0.42

Table B.10 Hole Diameter, Uncoated Tool at Vc=6.0 m/min

Hole Diameter (μm)					
Hole	Measurement 1	Measurement 2	Measurement 3	Average	Std Dev
1	141.70	140.39	142.35	141.48	0.81
5	140.51	140.20	140.44	140.39	0.13
10	143.15	143.88	142.13	143.05	0.72
15	147.93	149.74	150.65	149.44	1.13
20	145.40	145.41	143.87	144.89	0.73
25	144.41	145.39	141.48	143.76	1.66
30	146.08	151.02	145.27	147.46	2.54
35	142.65	144.97	144.63	144.08	1.02
40	142.53	142.46	141.88	142.29	0.29
45	143.46	141.73	141.04	142.08	1.02
50	140.67	140.48	142.59	141.25	0.96
55	143.16	145.14	140.02	142.77	2.11

60	142.96	141.56	144.04	142.85	1.02
65	143.97	145.53	142.80	144.10	1.12
70	139.51	143.57	142.14	141.74	1.68

Table B.11 Hole Diameter, Uncoated Tool at Vc=14.0 m/min

Hole Diameter (µm)					
Hole	Measurement 1	Measurement 2	Measurement 3	Average	Std Dev
1	145.76	145.46	145.48	145.57	0.13
5	150.11	143.28	147.28	146.89	2.80
10	146.00	145.41	146.84	146.08	0.59
15	146.06	148.85	147.66	147.52	1.14
20	149.73	147.14	151.39	149.42	1.75
25	147.44	148.04	146.53	147.34	0.62
30	147.37	145.70	144.44	145.84	1.20

Table B.12 Hole Diameter, Uncoated Tool at Vc=20.0 m/min

Hole Diameter (µm)					
Hole	Measurement 1	Measurement 2	Measurement 3	Average	Std Dev
1	147.647	145.8409	142.8303	145.4394	1.986788
5	155.0793	149.9938	151.3498	152.141	2.150225
10	145.265	145.8098	144.0091	145.028	0.753982

Table B.13 Hole Diameter, Nano-tek Coated Tool at Vc=3.2 m/min

Hole Diameter (µm)					
Hole	Measurement 1	Measurement 2	Measurement 3	Average	Std Dev
1	151.49	152.09	151.64	151.74	0.25
5	147.67	146.67	146.59	146.97	0.49
10	149.43	149.31	147.18	148.64	1.03
15	154.48	154.05	157.14	155.22	1.36
20	146.76	147.09	146.27	146.71	0.34
25	143.31	142.26	143.05	142.87	0.45
30	149.04	150.88	152.66	150.86	1.48
35	147.51	147.49	148.97	147.99	0.69
40	150.38	148.90	150.21	149.83	0.66
45	144.34	143.77	144.34	144.15	0.27
50	142.49	140.93	142.49	141.97	0.74
55	143.30	142.71	143.30	143.10	0.27

60	154.02	149.68	154.02	152.58	2.05
65	144.04	144.86	144.04	144.31	0.39
70	142.16	142.64	142.16	142.32	0.23
75	143.54	141.79	143.54	142.96	0.82
80	149.45	150.33	149.45	149.74	0.41
85	143.44	145.97	143.44	144.29	1.19
90	145.50	144.94	145.50	145.31	0.26
95	141.88	140.33	141.88	141.36	0.73

Table B.14 Hole Diameter, Nano-tek Coated Tool at Vc=6.0 m/min

Hole Diameter (µm)					
Hole	Measurement 1	Measurement 2	Measurement 3	Average	Std Dev
1	151.73	151.81	149.11	150.88	1.25
5	150.49	149.13	147.01	148.88	1.43
10	151.76	149.81	147.39	149.65	1.79
15	154.55	152.29	153.40	153.41	0.92
20	148.43	146.07	143.78	146.09	1.90
25	150.35	149.05	148.65	149.35	0.73
30	146.16	145.00	143.57	144.91	1.06
35	148.63	149.45	148.32	148.80	0.48
40	148.87	146.26	144.90	146.68	1.65

Table B.15 Hole Diameter, Nano-tek Coated Tool at Vc=14.0 m/min

Hole Diameter (µm)					
Hole	Measurement 1	Measurement 2	Measurement 3	Average	Std Dev
1	148.88	149.21	148.24	148.78	0.40
5	145.27	144.82	145.09	145.06	0.18
10	143.53	147.20	144.60	145.11	1.54
15	148.00	147.62	151.04	148.88	1.53
20	149.69	147.80	148.34	148.61	0.80
25	146.77	146.55	144.88	146.07	0.85
30	144.48	145.85	144.20	144.84	0.72
35	143.88	145.06	145.28	144.74	0.61
40	145.21	146.08	143.96	145.08	0.87
45	142.20	140.42	139.89	140.83	0.99
50	147.11	147.49	148.14	147.58	0.42
55	140.77	144.64	145.05	143.49	1.93

Table B.16 Hole Diameter, Nano-tek Coated Tool at Vc=20.0 m/min

Hole Diameter (μm)					
Hole	Measurement 1	Measurement 2	Measurement 3	Average	Std Dev
1	161.56	161.59	160.73	161.29	0.40
5	151.45	153.38	151.90	152.24	0.82
10	151.52	149.85	151.61	150.99	0.81
15	149.85	150.09	148.76	149.57	0.58
20	150.84	149.04	148.75	149.54	0.92

Table B.17 Hole Diameter, AlTiN Coated Tool at Vc=14.0 m/min

Hole Diameter (μm)					
Hole	Measurement 1	Measurement 2	Measurement 3	Average	Std Dev
1	149.17	147.68	147.52	148.12	0.74
5	145.70	143.89	144.18	144.59	0.79
10	145.50	146.82	144.32	145.55	1.02
15	149.34	151.58	149.72	150.22	0.98
20	146.46	149.43	148.60	148.17	1.25
25	145.30	143.80	144.57	144.56	0.61
30	139.87	143.79	142.34	142.00	1.62
35	146.88	144.26	143.90	145.01	1.33
40	143.53	145.32	143.49	144.11	0.85
45	140.25	139.47	141.55	140.42	0.85
50	145.96	145.89	148.37	146.74	1.15
55	145.23	147.09	143.61	145.31	1.42

APPENDIX C. COEFFICIENT OF FRICTION MEASUREMENTS

These tests utilized an inclined ramp of known angle θ, and timed the travel of a tool down a marked distance d = 30cm along the ramp. Twenty trials were completed for each of four different angles, and the average time for each angle calculated. Using these average times, the coefficient of friction could be calculated from Equation (C.7), and an average coefficient of friction for the entire experiment determined.

The net force on the tool is given by:

$$F_{net} = F_s - F_F \tag{C.1}$$

Where:

$$F_s = mg \sin\theta \tag{C.2}$$

$$F_f = \mu mg \cos\theta \tag{C.3}$$

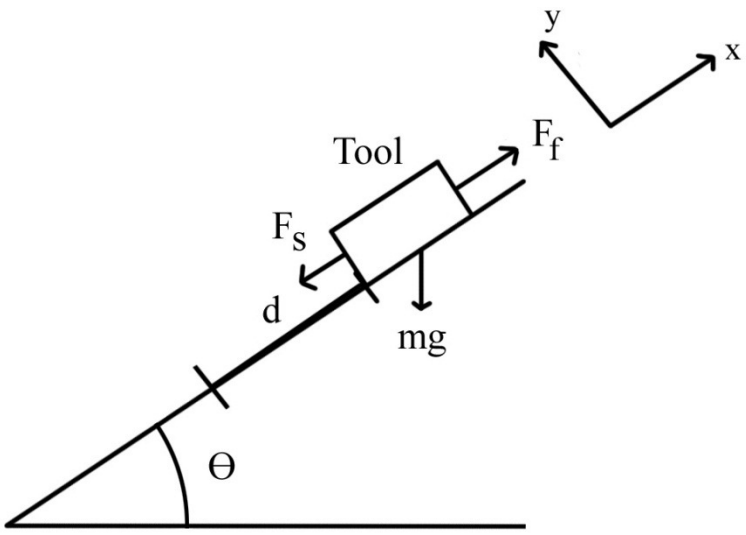

Figure 48: Free body diagram of a sliding tool on a Nitinol ramp

Therefore:

$$a_x = g \sin\theta - \mu g \cos\theta \tag{C.4}$$

Or,

$$\mu = \frac{g \sin\theta - a_x}{g \cos\theta} \tag{C.5}$$

From the kinematic equations, the acceleration of the tool can be related to its distance traveled and time by:

$$a_x = \frac{2d}{t^2} \tag{C.6}$$

So the coefficient of friction with no cutting fluid is given by:

$$\mu = \frac{g \sin\theta - \frac{2d}{t^2}}{g \cos\theta} \tag{C.7}$$

APPENDIX D. MICRO AND NANOHARDNESS TESTING DATA

Table D.1 Nanoindentation tests, AlTiN coated specimen

Measurement	hc(nm)	Pmax(μN)	S(μN/nm)	A(nm^2)	hmax(nm)	heff(nm)	Er(GPa)	H(GPa)
AlTiN_1b 0000	99.54	10051.83	158.63	343230.80	148.38	147.06	239.90	29.29
AlTiN_1b 0001	102.37	10046.50	188.29	360069.29	143.18	142.39	278.02	27.90
AlTiN_1b 0004	106.37	10040.51	165.23	384430.40	152.27	151.95	236.11	26.12
AlTiN_1b 0005	110.30	10045.10	175.86	409057.48	153.73	153.14	243.62	24.56
AlTiN_1b 0007	103.61	10047.21	192.24	367498.68	143.69	142.80	280.96	27.34
AlTiN_1b 0008	109.54	10044.73	162.68	404250.27	156.83	155.85	226.70	24.85
AlTiN_1c 0001	95.73	10053.93	157.66	321232.83	145.09	143.56	246.46	31.30
AlTiN_1c 0003	99.94	10045.85	165.77	345618.62	146.23	145.39	249.83	29.07
AlTiN_1c 0004	101.82	10045.14	170.79	356774.55	146.93	145.93	253.34	28.16
AlTiN_1c 0005	102.86	10042.63	172.22	362959.85	147.44	146.59	253.28	27.67
AlTiN_2a 0000	111.68	10047.06	172.21	417867.22	156.00	155.43	236.04	24.04
AlTiN_2a 0001	105.38	10046.27	172.93	378322.53	149.70	148.95	249.10	26.55
AlTiN_2a 0002	93.35	10046.70	170.68	307798.10	138.08	137.49	272.58	32.64
AlTiN_2a 0003	104.11	10044.78	173.06	370577.93	148.21	147.65	251.88	27.11
AlTiN_2a 0004	100.82	10044.93	183.26	350818.13	142.60	141.93	274.14	28.63
AlTiN_2a 0005	103.31	10045.24	176.82	365675.59	146.81	145.91	259.07	27.47
AlTiN_2a 0006	102.09	10043.75	176.56	358354.36	145.12	144.75	261.32	28.03
AlTiN_2a 0007	102.28	10046.70	173.32	359500.31	146.60	145.75	256.11	27.95
AlTiN_2a 0008	105.35	10045.57	173.01	378098.58	149.64	148.89	249.29	26.57
AlTiN_2b 0000	105.20	10049.01	173.30	377198.40	149.04	148.69	250.00	26.64
AlTiN_2b	102.56	10046.43	167.94	361194.25	148.39	147.43	247.58	27.81

0002								
AlTiN_2b 0003	101.95	10043.36	175.94	357543.66	145.28	144.77	260.69	28.09
AlTiN_2b 0004	105.75	10046.83	182.81	380569.86	147.17	146.97	262.56	26.40
AlTiN_2b 0005	99.06	10043.62	171.09	340439.09	144.04	143.09	259.81	29.50
AlTiN_2b 0006	103.33	10044.18	164.72	365839.69	150.29	149.07	241.29	27.46
AlTiN_2b 0007	98.60	10045.96	177.30	337787.80	141.94	141.10	270.28	29.74
AlTiN_2b 0008	105.67	10044.93	177.42	380072.77	148.76	148.13	254.98	26.43
Average	**103.06**	**10045.88**	**173.03**	**364547.45**	**147.46**	**146.69**	**254.26**	**27.68**
Std Dev	**4.05**	**2.63**	**7.99**	**24398.33**	**4.17**	**4.20**	**13.29**	**1.88**

Table D.2 Nanoindentation tests, Nano-tek coated specimen

Measurement	hc(nm)	Pmax(μN)	S(μN/nm)	A(nm^2)	hmax(nm)	heff(nm)	Er(GPa)	H(GPa)
Nanotek_1a 0002	107.0749	10046.5	176.6948	388772.2	150.4053	149.7183	251.0793	25.84161
Nanotek_1a 0003	90.678	10043.28	172.1354	293050	135.63	134.4369	281.7308	34.27155
Nanotek_1a 0005	110.2764	10048.11	176.2842	408903.2	153.9447	153.026	244.2519	24.57332
Nanotek_1a 0006	70.32924	10043.62	181.3526	191268.3	112.4667	111.8656	367.3982	52.51065
Nanotek_1a 0007	84.60135	10043.91	172.509	260693.1	129.2541	128.2682	299.3518	38.5277
Nanotek_1b 0000	100.0409	10050.92	167.7221	346200	145.6714	144.9855	252.5582	29.03212
Nanotek_1b 0002	97.01418	10042.47	179.6602	328579.8	139.5144	138.937	277.6939	30.56327
Nanotek_1b 0006	98.8269	10043.48	171.625	339082.1	143.359	142.7168	261.1337	29.6196
Nanotek_1b 0008	102.5555	10044	176.9145	361158.1	145.6374	145.1354	260.8252	27.81054
Nanotek_2a 0001	122.4555	10045.61	248.814	489818.5	153.65	152.736	314.9865	20.50885
Nanotek_2a 0002	78.20002	10043.21	223.0157	228417.9	112.853	111.9752	413.4329	43.96855
Nanotek_2a 0005	100.0096	10042.59	183.1236	346015.3	141.8325	141.14	275.8236	29.02355
Nanotek_2a 0006	107.8041	10045.38	172.2457	393315.9	151.8624	151.5442	243.3394	25.54023
Nanotek_2a 0008	156.7973	10047.88	195.341	755274	196.0074	195.3756	199.148	13.30363
Nanotek_2b 0000	76.19015	10048.37	179.2954	218666.2	118.9944	118.2229	339.7138	45.95301
Nanotek_2b 0001	89.07171	10043.22	166.8039	284333.6	134.6739	134.229	277.1577	35.32197
Nanotek_2b 0002	82.63167	10042.71	175.5775	250564.6	126.1434	125.5303	310.7734	40.08031
Nanotek_2b 0003	114.9121	10047.08	165.8703	438891.2	161.4341	160.341	221.8324	22.89197
Nanotek_2b 0004	115.2008	10044.4	215.3598	440792.3	150.8477	150.1809	287.3972	22.78715
Nanotek_2b 0005	74.18334	10042.77	169.9393	209110.9	119.0467	118.5055	329.2609	48.02604
Nanotek_2	110.3844	10046.19	177.737	40959	153.4811	152.	246.05	24.527

b 0007				0.8		7765	81	39
Nanotek_2 b 0008	89.39772	10042.88	167.8344	286093.2	135.2004	134.2762	278.0111	35.10352
Average	**99.0289**	**10044.94**	**182.5389**	**348572.3**	**141.4505**	**140.7238**	**283.3163**	**31.80848**
Std Dev	**19.45767**	**2.348584**	**20.72804**	**122980.5**	**18.65893**	**18.66168**	**48.7163**	**9.835333**

Table D.3 Microhardness tests, uncoated WC specimen

Measurement	Hardness (HV)
1	1917.2
2	1870
3	1865.3
4	1980.4
5	1907.4
6	1959.8
7	1971.4
8	1915.4
Avg.	**1923.4**
Std. Dev.	**41.0**

Table D.4 Calotest measurements, Nano-tek coated specimen

Measurement	X (µm)	Y (µm)	D (µm)	t (µm)
1	61.5	798.1	25795.28	1.903
2	61.2	797.8	25795.28	1.893
3	60	782.1	24773.25	1.894
4	51.7	790.4	24773.25	1.650
5	66.3	772.3	24295.12	2.108
6	55.7	761.7	24295.12	1.746
7	54.8	789.3	25314.67	1.709
8	55.9	790.4	25314.67	1.745
Average	58.39	785.26	25044.58	1.831
Std. Dev.	4.69	12.67	602.81	0.147